Tailoring powder strengths for enhanced quality of cold sprayed Al6061 deposits

Huang, Chunjie; List, Alexander; Shen, Junjun; Fu, Banglong; Yin, Shuo; Chen, Ting; Klusemann, Benjamin; Gärtner, Frank; Klassen, Thomas

Published in:
Materials and Design

DOI:
10.1016/j.matdes.2022.110494

Publication date:
2022

Document Version
Publisher's PDF, also known as Version of record

Materials & Design xxx (xxxx) 110494

Contents lists available at ScienceDirect

Materials & Design

journal homepage: www.elsevier.com/locate/matdes

Tailoring powder strengths for enhanced quality of cold sprayed Al6061 deposits

Chunjie Huang [a,*], Alexander List [a], Junjun Shen [b], Banglong Fu [b], Shuo Yin [c], Ting Chen [b], Benjamin Klusemann [b,d], Frank Gärtner [a], Thomas Klassen [a]

[a] Institute of Materials Technology, Helmut-Schmidt-University/University of the Federal Armed Forces Hamburg, 22043 Hamburg, Germany
[b] Solid-State Materials Processing, Helmholtz-Zentrum Hereon, Institute of Materials Mechanics, 21502 Geesthacht, Germany
[c] Department of Mechanical and Manufacturing Engineering, Parsons Building, Trinity College Dublin, The University of Dublin, Dublin 2, Ireland
[d] Institute of Product and Process Innovation, Leuphana University of Lüneburg, 21335 Lüneburg, Germany

HIGHLIGHTS

- Powder strength is reduced from 311 MPa to 179 MPa after soft annealing.
- Correlation of powder property and consequence for deposit property is derived.
- Single impact splat adhesion is revealed by cavitation-induced erosion.
- Powder-process-performance integrated cold spraying Al6061 is described.

GRAPHICAL ABSTRACT

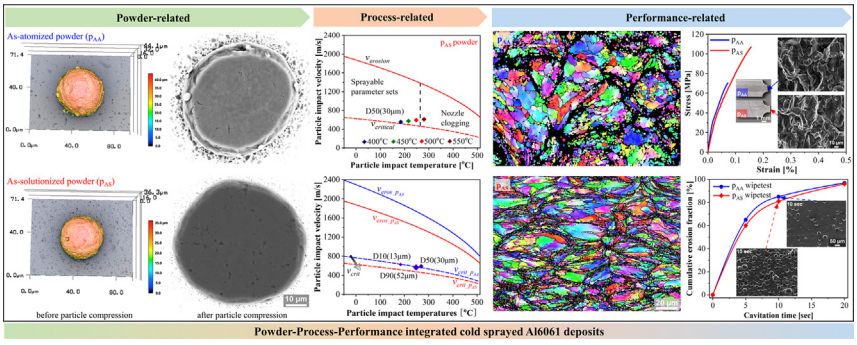

ARTICLE INFO

Article history:
Received 26 December 2021
Revised 11 February 2022
Accepted 24 February 2022
Available online 24 February 2022

Keywords:
Cold spraying
Al6061 powder treatment
Spraying parameters
Microstructural homogenization
Deposit mechanical properties
Single-particle adhesion

ABSTRACT

As verified by literature, heat-treatments of as-atomized Al-alloy powders before cold spraying, result in microstructural homogenization and deposition efficiency increment. So far, a straightforward correlation between powder strength and consequences for the performance in cold spraying and deposit properties is still missing. This work thus provides reliable analyses of powder strengths in as-atomized and annealed states to the calculation of critical velocities and deposit quality parameter η, as well as the associated influences of powder strength on single-particle adhesion and deposit microstructures and properties. By annealing of as-atomized powder, its strength is reduced by about 60%, which allows decreasing the critical velocity for a successful deposition. Experimental results demonstrate that powder strength-based calculation of quality parameter η allows for a more realistic description of microstructural characteristics and deposits properties. The single-particle impact morphologies as well as the detachment features of adhering splats by cavitation tests visualize the respective deposition characteristics and bonding behaviors. The lower critical velocities by annealing contribute to better single splat adhesion, lower porosity, higher electrical conductivity, as well as improved tensile strength of deposits. The direct correlation of powder pre-annealing and strength in combination with cold spraying parameter variation allows defining effective strategies for improving deposit properties.

* Corresponding author.
E-mail address: huangc@hsu-hh.de (C. Huang).

https://doi.org/10.1016/j.matdes.2022.110494
0264-1275/

1. Introduction

Cold spraying (CS) is a solid-state deposition process, where micron-sized metallic particles are accelerated to high velocities by a pressurized and heated gas jet [1–6]. Particles that impact onto the substrate or already deposited spray layer at a velocity v_p that exceeds their material and size-dependent critical velocity v_{crit} will bond by locally occurring severe plastic deformation and associated adiabatic shear instabilities, which means thermal softening compensating all sorts of hardening effects [2,7,8]. The v_{crit} can be calculated according to [2,3], as

$$v_{crit} = 0.5\sqrt{16\frac{UTS}{\rho_p}\left(\frac{T_s - T_p}{T_s - T_{ref}}\right) + c_p(T_s - T_{imp})} \quad (1)$$

by combining mechanical contributions including particle ultimate tensile strength (UTS), density (ρ_p) and thermal contributions as specific heat (c_p), softening or melting temperature (T_s) and particle impact temperature (T_{imp}).

Summing up, if being sustained to identical particle impact conditions (with respect to particle velocity v_{imp} and particle temperature T_{imp}), the inherent characteristics of the sprayed powder, such as its microstructures (grain sizes, dislocation densities, phase contents and distributions, etc.) and associated mechanical properties (strength, hardness, etc.), play a critical role for attainable qualities of metallic deposits [7,8]. Due to powder production routes and individual thermal–mechanical histories [9], however, powder feedstocks of the same materials composition can exhibit rather different microstructures and thus properties. Already finer grain sizes by fast solidification during inert gas atomization lead to higher strength as compared to corresponding softening annealed bulk materials. Particularly for aluminum alloy powders produced by inert gas atomization, far-from-equilibrium microstructures and fine grain sizes are obtained by associated rapid solidification [10–16]. In addition, solute segregation at interdendritic boundaries can increase the hardness and strength of the produced powders [11,13]. Such possible solute segregation could result in inhomogeneous strength distribution within spray particles, here close to grain boundary areas having higher strengths due to a higher super-saturation with solute atoms. This could cause inhomogeneous features during impact and deformation.

Non-equilibrium and cellular dendritic microstructures as well as possible solute segregation cover only part of the story. Many Al alloys already at room temperature naturally age by the formation of nano-precipitates and increase their strength (usually described by T4 in temper descriptions). Such natural aging could be enhanced by locally higher super-saturation and thus thermodynamically higher driving forces for nucleation and growth. A major influence will be given by powder storage time and temperature. Therefore, knowledge of real Al-alloy powder microstructures and powder strengths is a necessary prerequisite for understanding the performance in CS.

Aiming to reduce or nearly to eliminate the alloying element segregation and to dissolve possibly formed precipitation in gas-atomized Al alloy powders, solution heat-treatments were used to homogenize the microstructure before deposition [10,11,13–16]. The already existing studies on annealing of Al alloy powders, as well as the corresponding process parameters and deposit performances for cold spraying, are summarized in Table 1. For example, Rokni et al. [10] applied a heat-treatment at 400 °C for 6 h on gas-atomized Al5056 powder. Such treatment led to the dissolution of Mg segregations into the Al matrix. As a consequence, the powder got softer and the formation of adiabatic shear instabilities (ASI) became more prominent during the impact. Sabard et al. [11] observed the rearrangement of the original dendritic microstruc-

Table 1
Summary of literature on Al-alloy powders heat-treatment, i.e. annealing, and spraying parameter related performance of cold sprayed deposits. *SHT: solution heat-treatment, p_{AA}: as-atomized powder, p_{AS}: as-solutionized powder, Q: quenching.

Powder	SHT* conditions	Powder characteristics	CS process, conditions	Performances	Ref
Al7075	450 °C for 4 h	• Cellular phases dissolve into Al matrix. • Hardness decreases from 101 to 75.2 HV.	He (2.9 MPa, 25 °C)	• p_{AS}* leads to more severe deformation by visible jetting and also thicker coatings.	[12]
Al6061	530 °C for 4 h	• Cellular microstructure in powder is eliminated. • Particle hardness decreases from 105 to 82.5 HV.	He (2.9 MPa, 25 °C)	• p_{AA}* coating shows a homogeneous distribution of strain and misorientations in the whole deposit. • p_{AS} coating appears strain-free at the particle centre while showing larger misorientation at its peripheries.	[13]
Al6061	400 °C for 2 h + 530 °C for 0.5 h	• Mg-Si and Fe-Si-Al secondary phases are identified at the cellular boundaries. • Homogenized powder shows higher flow stress.	He (3 MPa, 380 °C)	• Yield stress of splats is not dependent on the initial powder structure. • Splat ductility is dependent on the initial powder state.	[7,16]
Al5056	400 °C for 6 h	• Homogenous distribution of Mg solute in Al matrix after SHT.	He (2.8 MPa, 400 °C)	• Heat-treated powder causes better adhesion, as well as higher UTS and ductility of the deposit.	[10]
Al7075 Al2024 Al6061	498 °C for 2.5 h + Q*	• Designed SHT method appears as effective for gaining more homogeneous Al alloy powder microstructures. • Cellular microstructure is dissolved to solid solution after HT	He (3.2 MPa, 415 °C)	• p_{AS} coatings exhibited more homogenous microstructures. • DE of Al7075, Al2024 and Al6061 powders is improved from 35 to 59%, 49 to 66%, and 71 to 89%, respectively.	[14]
Al-2CuAl-5Cu	535 °C for 2 h	• θ-phase at cell boundaries is removed after SHT. • Cu content is increased in Al-matrix after SHT. • Grain sizes are increased by SHT.	N_2 (3.79 MPa, 400 °C)	• SHT powders exhibit higher DE, but less increase for higher Cu content powder. • Coating porosities are increased using SHT powder, e.g. from 2.9 to 6% for Al-5Cu, probably due to insufficient deformation.	[15]

tures, leading to a decrease in microhardness from 101 to 75 HV in solutionized Al7075 powder (450 °C for 4 h + water quenching). As consequence, distinct increases in deposition efficiency (DE) from 8.6% to 50% and deposit thickness from 40 to 300 μm were obtained. In another work, Sabard et al. [13] indicated that the solution treatment at 530 °C for 4 h + water quenching gave rise to a rather more intimate bonding between the inter-splats. Aiming to prevent the possible powder sintering/oxidation during annealing and re-precipitation during cooling, Story et al. [14] constructed a furnace (gas-protection + brine bath) for solutionizing different types of Al-alloy powders. The sprayed deposits processed by helium at T_{gas} = 415 °C, p_{gas} = 3.2 MPa using the heat-treated Al7075 powders resulted in a DE of 59%, being substantially higher than the DE of 35% by using the as-atomized powder. For Al2024 and Al6061, the DE was raised from 49% to 66%, and from 71% to 89%, respectively, as compared to the use of untreated powders. However, the oxygen contents of powders were not analyzed after these treatment procedures [14]. Following the annealing procedure for Al powder developed by Story et al. [14], Liu et al. [15] reported a 2.8-fold growth of the originally fine grain sizes of gas-atomized Al-Cu powders by solutionizing at 535 °C for 2 h and cooling at 5 °C/s. This led to an about 3.5-fold increase of the DE.

Due to the reduced microhardness and strength of as-solutionized powder [11,13], the critical velocity allowing for effective bonding during particle impact will be lower as compared to the as-atomized feedstock [8]. To supply further understanding on influences of initial microstructures, Flanagan et al. [7] and Bedard et al. [16] studied the effects of homogenization at 400 °C for 2 h + 530 °C for 30 min of Al6061 on particle properties of the respective feedstock particles and single impact splat features by in-situ micropillar compression testing. Two main, on first view contracting conclusions were obtained, i) the as-atomized particles showed a yield strength of about 190 MPa, whereas the particles after heat-treatment showed a higher strength of 229 MPa; ii) however, cold sprayed splats of as-homogenized particles exhibited a higher ductility, indicating that the initial powder microstructure determined a better ductility of splats. The observed increase in yield strength after powder annealing and homogenization treatments [7,16] can be explained as follows: in as-atomized and partitioned conditions, the solute atoms and precipitations are more prominently located at grain boundaries. Thus, the particle interior being objected to micropillar testing is less solution hardened. By a solution treatment, the segregations distribute as solutes to the grain interior and cause solution hardening, thus increasing the overall yield strength. Aiming to investigate the phase evolution during thermal treatments, Tsaknopoulos et al. [17] annealed Al6061 powder at 530 °C for 1 h, and concluded that it was not possible to achieve a fully homogenous microstructure, since occurring Fe-rich phases grow whereas the Mg_2Si-precipitates dissolve.

As stated by Eq. (1), the key factor to influence v_{crit} of a powder feedstock is the powder strength. Thus, for the designed tuning of cold sprayed deposits, essential knowledge of powder particle strength under associated heat-treatments is needed. However, the state of the art demonstrates that local indentation techniques, i.e. micro-and nano-hardness methods, are generally associated with the drawbacks, such as the systematic errors by resin deformation or surface oxides, as well as the large scatter by the differences in local microstructures. For supplying a more comprehensive view on influences by powder annealing or other modification techniques, the present study evaluates more global properties as overall particle strength on the deformation behavior during impact in cold spraying and attainable deposit properties. For this comparison, an as-atomized and stored Al6061 powder was solutionized at 500 °C for 1 h. The influence of solutionizing on powder strength was investigated by particle compression testing, supplying information on global deformation behaviors. Based on powder strength data, a more realistic quality parameter η, defined as the ratio of particle impact velocity v_{imp} to the critical velocity v_{crit} at individual impact temperatures [3,4,8],

$$\eta = v_{imp}/v_{crit} \quad (2)$$

was obtained. Based on particle impact velocity and critical conditions for bonding, the deposit quality parameter η is considered to provide an all-inclusive, dimensionless description for CS deposit properties. As long impact temperatures do not approach the melting temperature of the powder material, the quality parameter η allows for correlations with deposition efficiencies, microstructural characteristics as porosity as well as physical material properties, such as UTS, electrical conductivity and also microhardness [3].

Al 6061 is commonly used for a wide range of applications [16]. The success of solid-state powder deposition for applications of functional coatings or structural repair is often impaired by non-sufficient deformability of the powder feedstock. Unexpected high powder strength could be due to non-sufficient cooling conditions in powder production or natural aging during storage. So far, only few reports are available that discuss the direct influences of powder conditions onto powder strength and consequences for success in cold spraying. To shed more light into needed procedures, the present study seeks to combine subsequent analyses of spray powder and possible modification to obtained deposit qualities in cold spraying by taking Al6061 as an example, that particularly might suffer from natural aging.

For providing a comprehensive study, various effects are analyzed. Thus, the study contains information about effects by powder solutionizing and strengths on the deposit microstructures and properties, as well as the deformation behavior of individual single particles and respective splat adhesion by cavitation testing to gain more information on bonding mechanisms. The general concepts should be transferable to a variety of feedstock material used in cold spraying. For the given example of Al6061, benefits are expected for layer deposition, but more prominently for structural restoration of components by demonstrating the practicability of microstructural adjustment for CS via powder heat-treatments. In addition, the results might promote the cost-effective production via cold spray additive manufacturing by using nitrogen as process gas.

2. Materials and methods

2.1. Materials

All the samples were fabricated using one batch of gas-atomized Al6061 powder (TLS Technik, Germany) kept under powder storage (>5 years) at ambient temperature in the original Ar-packing atmosphere. The powders were processed by using the EIGA-technique for ensuring spherical morphologies. Analyses by using laser scattering (LA-910 Horiba, Japan) was used to reveal the powder size distributions (PSD). The powder was assorted in two batches before spraying, i.e. powder for solution heat-treatments (referred to as p_{AS}) and the as-atomized and stored state (referred as p_{AA}) for comparison. The solutionizing treatment of the initial Al6061 powder particles was conducted at the temperature of 500 °C for 1 h in a high-vacuum oven of type VHT8/18-KE, Nabertherm, Germany under a vacuum of 2×10^{-6} MPa. Quenching was applied by N_2 flow at a cooling rate of 10 °C/min after the solution heat-treatment. The powder morphologies were analyzed by scanning electron microscopy (SEM, Quanta 650, FEI, Netherlands) in secondary electron (SE) mode.

The individual oxygen contents of the two batches were examined by using an analyzer type G8 Galileo from Bruker, Germany.

$AlMg_3$ (a 5xxx series aluminum alloy) plates with a microhardness of 62 $HV_{0.3}$ were used as substrate (dimension of 50 × 70 × 3 mm for processing deposits and of 50 × 20 × 3 mm for performing the wipe tests to collect single particle impacts). The substrate surfaces were grit-blasted by using Al_2O_3 for obtaining thick deposits for complete layer analyses and prepared to a mirror-like polish finally applying oxide polishing suspension (OPS) for processing the wipe tests.

2.2. Particle strength analyses by compression tests

The particle strength was measured by using the particle compression method, as schematically illustrated in Fig. 1a and described by Assadi and Gärtner [8]. In the case of annealed powders, these tests were performed directly after solutionizing treatments to avoid the effects of natural aging. Before and after the compression testing, particle shapes and sizes (i.e. particle diameter d_p and particle height h_p) were analyzed using confocal laser scanning microscopy (CLSM, VK-X20, KEYENCE, Germany). After compression, SEM was used to analyze the deformed morphologies and microstructures. Fifteen particles were tested for each of different powder conditions.

Compression testing was conducted on a modified instrumented microhardness testing machine (ZHU0.2, Zwick Instruments, Germany) with a flat diamond head (200 μm in diameter). The particles were placed individually on a hard metal (WC-Co) base plate (HM-plate GD10, DURIT Hartmetall, Germany) with the dimensions of 25 × 70 × 5 mm^3 to avoid any influence by the experimental setup. Compression testing was performed displacement-controlled under a rate of 0.1 mm/min until reaching a maximum load of 1.1 N, as roughly estimated by a role of thumb (rewritten Eq. 5 in [6]) by assuming max. particle sizes under investigation and bulk strength data (T0 / T6 temper). A displacement of > 50% is needed to guarantee a sufficiently large range of plastic deformation occurring during deformation for later curve fitting. The obtained raw force–displacement data were transformed to corresponding nominal stress vs. strain curves [6,8]. The authors proposing the method used FEM modelling for parameterizing the complex stress and strain states during compression of a sphere into a simple Johnson Cook expression $\sigma = A + B\varepsilon^n$ with the stress σ as function of yield strength A and strain hardening $B\varepsilon^n$ [6,8]. With the parameterized function in the background, the A, B and n as Johnson - Cook parameters are then obtained by applying fitting procedures to the experimental data. More details of force and yiled stress determination are given in section 1 of the supplementary material.

2.3. Calculation of impact conditions and critical velocities in cold spraying

The critical velocity for reaching successful deposit formation strongly depends on the feedstock powder strength, as given in Eq. (1). The different critical velocities, as well as the respective particle impact conditions (impact velocity v_{imp} and impact temperature T_{imp}) were investigated by applying KSS software (Kinetic Spray Solutions, Germany) [4]. Details on the principles are described in [2,18]. By using the powder strength extracted from experimental results as the input data, a more realistic description of the deposit quality parameter η, can be obtained. As a result, better-defined correlations between spray parameters and deposit characteristics and deposition efficiencies can be derived. The respective influences are summarized for CS deposition given in Fig. 2.

2.4. Cold spraying

The samples for the single-impact wipetests and the full deposits were produced with a commercial CS system of type Impact 5/11 (Impact Innovations, Germany) by using a convergent-divergent nozzle type SiC-Out1 (Impact Innovations, Germany) in combination with a 35 mm pre-chamber extension. Nitrogen was used as the process and carrier gas. Particularly for Al-alloys, the process gas temperature is considered as the most important parameter, as its increase leads to higher particle velocities and promotes thermal softening of spray particles. Both result in more extensive deformation and better bonding. For correlating the corresponding particle impact conditions to attainable deposit properties for the softening annealed powder, the process gas temperatures (T_{gas}) were systematically varied in a range from 400 to 550 °C, while keeping the gas pressure (p_{gas}) constant at 3 MPa. For the hard and naturally aged powder, p_{AA}, the reference experiment was performed at T_{gas} = 500 °C and p_{gas} = 3 MPa. For attaining full deposits and single impacts by wipe tests, secondary parameters were kept fixed with line traverse speeds of 250 and 750 mm/s and powder feeder rotation speeds of 3 and 0.5 RPM, corresponding to feed rates of 14.2 and 2.4 g/min, respectively. Detailed calculations see Supplementary Material section 2. The full deposits were built up to a thickness of a minimum 1.1 mm to ensure dimensions that allow for the preparation of micro-flat tensile (MFT) testing samples. The stand-off distance was kept

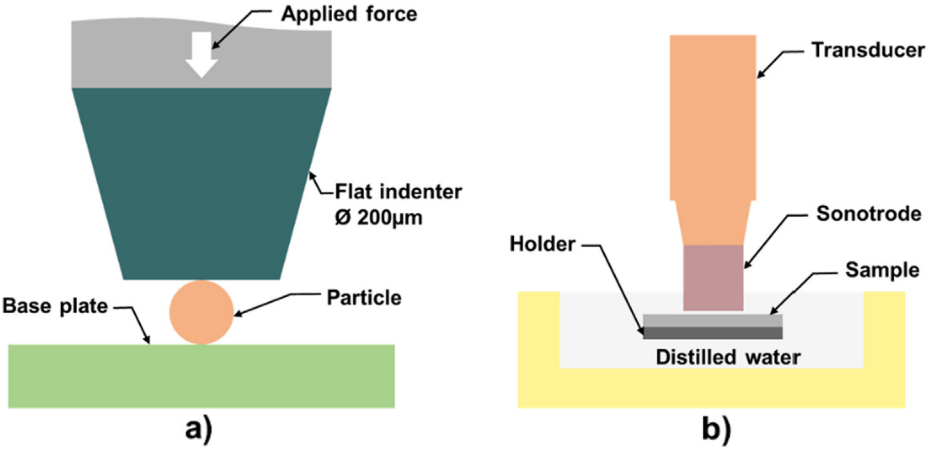

Fig. 1. Schematics of experiment setups: (a) particle compression testing, and (b) cavitation testing.

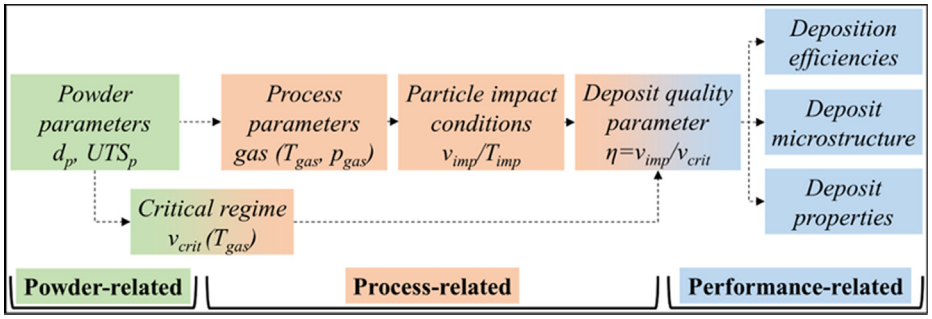

Fig. 2. The layout of powder-process-performance integrated cold spraying deposition.

Table 2
Cold spray parameters for CS Al6061 deposits and wipe test samples in this work.

Samples	Processing gas	T_{gas} (℃)	P_{gas} (MPa)	Standoff distance /mm	Gun traverse speed/ mm	Powder injection distance (mm)	Feed rate (g/min)
p_{AS} deposits	N_2	400450500550	3	30	250	35	14.2
p_{AA} deposit		500					
p_{AS} wipetest	N_2	500	3	30	750	35	2.4
p_{AA} wipetest							

fixed at 30 mm in all experiments. The whole set of parameters of this work is summarized in Table 2.

2.5. Microstructural and chemical characterization

Cross-sections of particles and deposits after the grinding procedure were firstly prepared by using diamond suspension and in the last step polished using OPS solution for revealing microstructural differences. Deposit microstructures and porosities were determined by cross-sectional observations, using an optical microscope (OM) of type DMRM in combination with the AxioVision analysis software (Leica, Germany). The backscattering electron (BSE) mode of the SEM of type Quanta 650 (FEI, Czech Republic) was used to reveal microstructural details as grain morphologies and secondary phases. To obtain additional information on the effects of powder annealing on the plastic deformation behavior in the deposits, the local microstructures in the centre of the deposits were analyzed by using EDAX electron backscattering diffraction (EBSD). EBSD analyses were performed on a Quanta 650 field-emission SEM (FEI, USA) equipped with an EBSD system. The data were analyzed by software TSL OIM (EDAX, USA). The accelerating voltage and the current were set to 20 kV and 5nA, respectively. EBSD mapping was performed with a step size of 0.2 μm, and the scanning area was set to 175 × 137 μm^2. The oxygen contents of powders and coatings were determined by inert gas fusion instrument (G8 Galileo, Bruker, Germany).

2.6. Electrical conductivity measurements

The electrical conductivity of full deposits was determined by using a Sigmascope SMP 10-HF device and a sensor type ES40HF (Helmut Fischer, Germany). The experiments were conducted following ASTM-standard E1004 using an inductive method. To reach low penetration depths of less than 250 μm, a frequency of 1250 kHz was used. To distinguish the possible influences of surface topographies on the in-plane conductivity, the tests were performed on as-sprayed and polished surface states. The obtained results were averaged from ten individual measurements to ensure sufficient statistical reliability. As reference, a cold rolled bulk Al6061-T6 plate with a thickness of 3 mm was analyzed as well.

2.7. Hardness testing

Deposit microhardness was measured in through-thickness positions on the polished cross-sections according to ASTM E384-10 standard. For each sample, twenty indentations were randomly obtained using a universal hardness testing machine of type ZHU0.2 (Zwick/Roell Instruments, Germany) at room temperature with a Vickers indenter under a load of 2.942 N ($HV_{0.3}$) using a dwell time of 10 sec.

2.8. Testing of deposit mechanical properties

For performing MFT tests, respective samples of the different deposits produced at T_{gas} = 500 °C were compared. The samples were extracted parallel to the nozzle movement direction by wire spark erosion. In order to reduce the hardening effect by natural aging extraction and testing was performed soon after CS, usually within one week. For the analysis of mechanical properties of the deposits, five MFT specimens of gauge dimensions with a length of 9 mm, a width of 2 mm and a thickness of 1 mm were evaluated. The tensile testing was carried out on a tensile testing machine of type Z100 (Zwick/Roell, Germany) at an increasing force rate of 2 N/sec until the complete fracture of the sample. After failure, the fracture morphologies were observed using the SE mode of the SEM.

2.9. Determination of single-particle adhesion by cavitation testing

To investigate details of particle-to-substrate adhesion and associated bonding mechanisms, cavitation tests were performed on the wipe test samples by applying a test rig of type BK101Z (KLN Ultraschall, Germany). According to ASTM G32-10 by applying the indirect mode with a sonotrode having a diameter of 15 mm, the test was conducted at an amplitude of 25 μm and applying a frequency of 20 kHz [19]. The samples were kept at a distance of 0.5 mm to the sonotrode, as illustrated in Fig. 1b. Surface topographies were subsequently investigated by SEM in the initial state and after 5, 10, and 20 sec of cavitation test duration. After cavitation, the removed single splats were extracted by filtering the liquid used for cavitation testing. After drying the filter

paper, the detached particles were transferred to the conductive adhesive of pre-prepared SEM-stubs (see Supplementary material, section 3) and then analyzed by SEM in SE mode. The size analyses for craters and single splats left in the substrate surface were performed via image-processing (ImageJ 4 1.51a, NIH, USA).

3. Results

3.1. Influence of solution heat-treatment on powder microstructure and properties

3.1.1. Surface morphologies and size distributions

Results concerning possible influences of the solution heat-treatment on the surface morphology and size distribution of the stored Al6061 powders are presented in Fig. 3. The individual particles, before and after solutionizing, exhibit spherical shapes with a rather smooth surface, as shown by the SEM micrographs in Fig. 3a-b. Only a few of the larger particles show some satellites, as denoted by black arrows in insets of Fig. 3a-b. According to the powder morphologies given in Fig. 3b, the heat-treatment does not lead to powder sintering, which is in agreement to the particle size distributions shown in Fig. 3c.

The unimodal size distributions given in Fig. 3c for powders p_{AA} and p_{AS} are rather similar with mean populations D50 at 29.6 μm and 30.3 μm, respectively. For calculating the particle impact conditions and critical velocities, the sizes according to D10, D50 and D90 corresponding to 13, 30 and 52 μm, respectively, were used. Due to the heat-treatment, oxygen content slightly increased from 0.09 wt% of p_{AA} to 0.13 wt% of p_{AS}, indicating that oxidation could not be completely avoided during the vacuum heat-treatment [14,15]. The oxygen contents can be mainly attributed to oxide films being present after storage and slight growth during annealing [20,21].

3.1.2. Particle microstructures

Examples of powder microstructures in as-atomized/stored and annealed states are given in Fig. 4. Fig. 4a-b show the cross-sectional microstructures of single p_{AA} particles, as observed by SEM in BSE contrast level, which illustrate a rather spherical shape and absence of porosity. In the as-atomized state p_{AA}, the powder comprises distinguished cellular (Fig. 4a) or dendritic (Fig. 4b) microstructures [10,11]. In the BSE contrast, solute segregations, appearing as light grey contrast, can be observed at cell or grain boundaries, which can be distinguished against the dark grey contrast of the Al-matrix in the grain interiors.

In order to dissolve possible nano-precipitates formed during room temperature storage and to homogenize microstructural segregation features from atomization, Al-alloy materials are generally heat-treated for a certain time by exceeding a temperature of 500 °C (but staying below the solidus of 595 °C) and then quenched with defined cooling rates [22]. The micrographs in Fig. 4c-d demonstrate that the heat-treated powder shows microstructural rearrangements, so that solidification textures can no longer be identified. This includes a possible rearrangement of former cell boundaries to grain boundaries. In addition, as indicated by the lower contrast of boundaries, solute segregation seems to be significantly reduced.

3.1.3. Particle strength

The heat treatment was applied to obtain microstructural homogenization by the dissolution of nano-precipitates and boundary segregations in a supersaturated α-Al matrix, and thus a reduced powder strength. Fig. 5 summarizes respective results from particle compression tests. Fig. 5a shows representative force–displacement curves of p_{AA} and p_{AS} powders, clearly illustrating the differences in the deformation behaviors of the as-atomized/stored and the heat-treated powders.

The force–displacement data from particle compression testing were converted to the nominal stress–strain curves (Fig. 5b) by using the fitting procedure described in [8] to gain information on yield strength (YS) and UTS. For the as-atomized and subsequently stored particles, YS, UTS, and YS/UTS ratios were determined to 151 MPa, 311 MPa, and 0.49, respectively. After heat-treatment, YS, UTS and YS/UTS ratio of the Al 6061 powders were reduced to 77 MPa, 179 MPa and 0.43. In the following (see section 3.3), mean UTS values will be used for the calculation of the critical velocities v_{crit}, thus guaranteeing a more reliable forecast and interpretation of the deposit quality parameter η.

3.1.4. Powder morphology during compression testing

Fig. 6 shows top views of selected particles before and after deformation as obtained by confocal microscopy. It reveals approximately spherical shapes for p_{AA} and p_{AS} particles in the initial, undeformed states, as shown in Fig. 6a-b, and 6e-f. After deformation, the top view of the p_{AA} particle in b) indicates a slightly ellipsoid deformation morphology. This can be explained by the

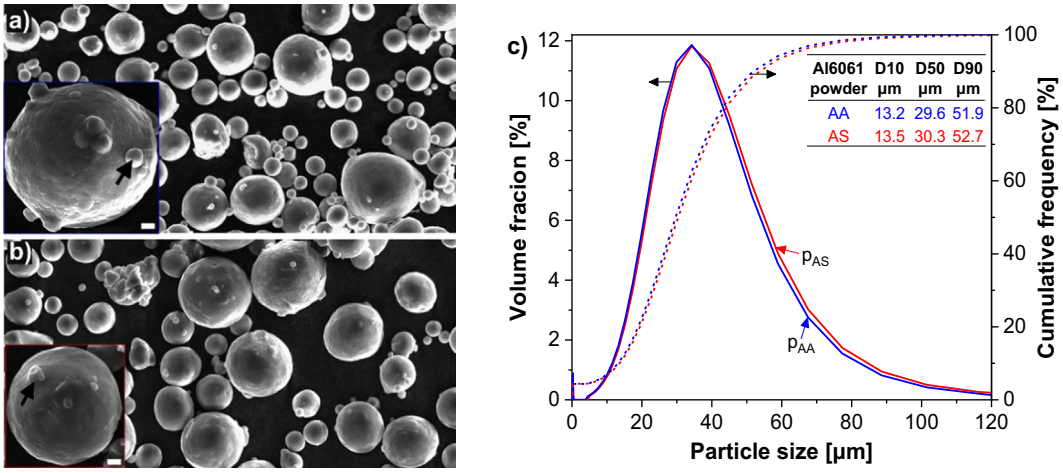

Fig. 3. Al6061 powder morphologies obtained by SEM: (a) as-atomized (referred as p_{AA}) and (b) solutionized (at 500 °C for 1 h, referred as p_{AS}), the insets of SEM images at higher magnification show some details with particle satellites. The scale bars in the inserts represent 5 μm. (c) Particle size distributions measured by laser scattering. The blue and the red solid and dashed curves represent populations and cumulative size distributions of the p_{AA} and p_{AS} powders, respectively. The inserted table shows the mean values of D10, D50 and D90, referring to sizes for 10%, 50% or 90% volume content of the whole size distribution.

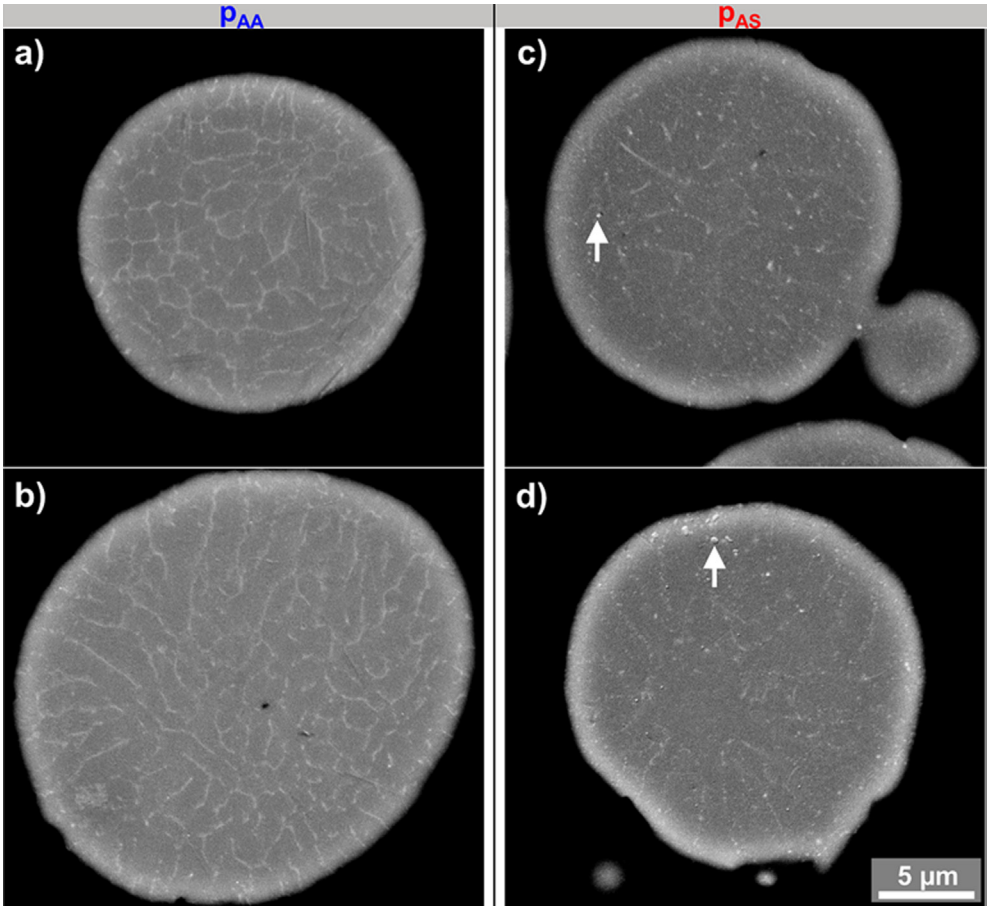

Fig. 4. Cross-sectional micrographs of single Al6061 particles by SEM in BSE mode: (a-b) as-atomized and (c-d) as-solutionized. The light grey contrast reveals the presence of alloy elements in interdendritic areas or the grain boundaries by partitioning, as distinguished against the dark grey appearing Al matrix. The white arrows indicate the Fe-rich phases.

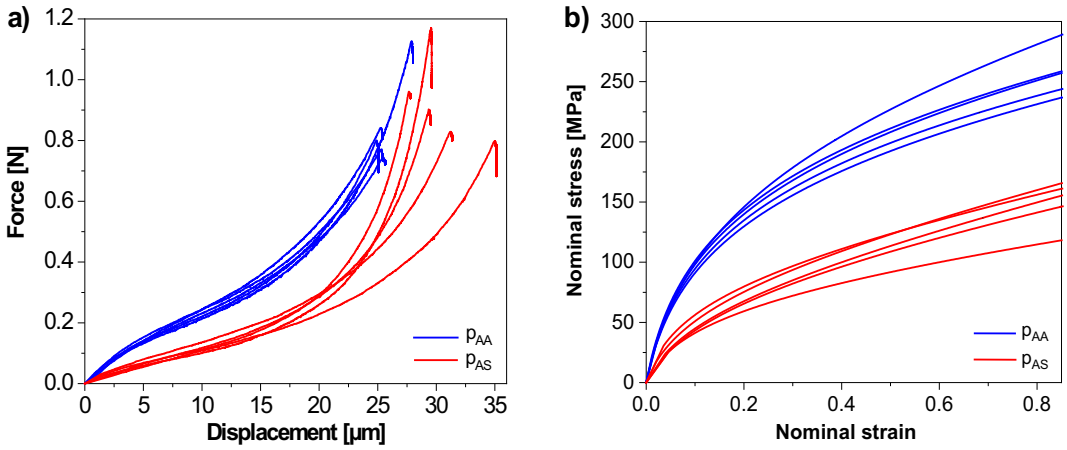

Fig. 5. Deformation during Al6061 particle compression tests: (a) selected raw force–displacement curves of as-atomized (p_{AA}) and as-solutionized (p_{AS}) powder particles; (b) the corresponding nominal stress vs. nominal strain curves, converted from the raw force–displacement data of (a) using the calculation method from [8].

differences in crystallographic orientation and inhomogeneous, anisotropic plastic deformation of larger grains. In addition, the top views reveal the dendritic and cellular solidification microstructures on the deformed surfaces (see black arrows in Fig. 6c and 6d)

Although a more homogenous microstructure can be achieved by the solution heat-treatment using a higher temperature or a longer treatment time, the growth of a Fe-rich grain boundary phase cannot be avoided [17]; see also initial Fe-rich phases getting present after the performed heat-treatment in Fig. 4c-d. The Fe-rich phase can act as potential crack nuclei and reduce the mechanical properties of the deposits. This means that inappropriate employment of heat-treatment on Al6061 powder can lead to reduced performance in powder deformation. In addition, fracture

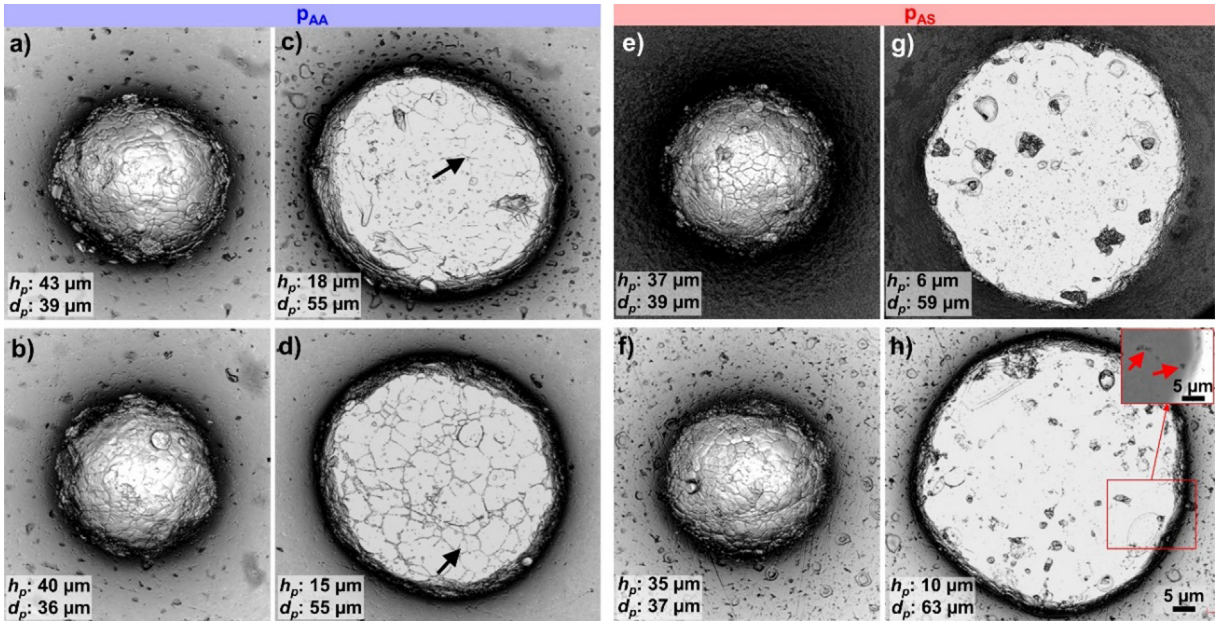

Fig. 6. Particle compression test morphologies of Al6061 particles: (a-d) p_{AA} and (e-h) p_{AS}. Confocal micrographs in (a, b, e and f) show details at a top view before compression. Particle morphologies microstructures after deformation as analyzed by confocal microscopy are given in (c, d, g and h).

of brittle oxides at grain boundaries or the surface could limit powder deformation as already observed during the compression test (see red arrows in the inset of Fig. 6h). According to the deformation morphologies, the p_{AS} particles in Fig. 6c-d reveal a less anisotropic behavior than the p_{AA} particles (Fig. 6g-h).

Since the particle impact behavior in CS strongly depends on powder properties, particle compression demonstrates 'best practice' to allow for predicting possible properties of attainable deposits and to derive more general correlations. For modifying the spray feedstock, at the same parameter sets, better deposit properties can be expected by using softening annealed powders. Such softer particles will result in low porosity and high cohesive strength by attaining more well-bonded interfaces [18].

3.2. Deposition optimization of CS Al6061

This section describes the parameter selection to develop Al6061 deposits that by microstructural optimization and lower strengths allow for better deposit properties. Such is needed to operate within spray parameter regimes that avoid nozzle clogging, and thus guarantees better process stability. Calculations by KSS software supplied the impact conditions under individual spray parameter sets and the respective critical conditions for bonding as the window of deposition (WoD) for CS [2,3], as given in Fig. 7. This allows for a better understanding of the influences by different process gas temperatures on the deposit quality parameters η. For p_{AA} and p_{AS}, the related data for the mean sizes (D50) are given in inserts of Fig. 7a, b. The comparison shows that, for each spray parameter set under investigation, the individual particle impact conditions strongly depend on the process gas temperature. With the gas temperature regime ranging from 400 up to 550 °C, the particle impact temperatures were varied in a wide range from 184 to 280 °C, while particle velocities differ less in the range from 553 to 610 m/s. It is worth noting that, all calculated impact conditions under the applied spray parameter sets exceed the critical conditions for bonding. As a result, the individual η values for the annealed powder (p_{AS}) were derived to range from 1.07 up to 1.35 with increased particle temperatures. Generally, a η-value of 1.07, as obtained at a gas temperature of 400 °C, means that the particle velocity is only slightly higher than the critical velocity and should result in a high porosity and low performance of the respective deposit [8,18]. By increasing the gas temperatures to 500 and 550 °C, η-values of about 1.25 and 1.35 were obtained, thus leading to better deposit properties.

Although a short powder injection distance of 35 mm upstream nozzle throat was selected, the problem of nozzle clogging at T_{gas} = 550 °C was yet not completely avoided during CS. Thus, for spraying Al6061 powder, a temperature of T_{gas} = 500 °C was regarded as optimum in the present work to guarantee the needed process stability. According to the literature, this process gas temperature of 500 °C represents the upper regime for spraying Al materials, regardless of using N_2 or He as a processing gas [10,14–16]. In most cases, lower process gas temperatures were used for CS with, for instance, Al5056 at 400 °C [10], Al2024, Al6061 and Al7075 415 °C [14], Al-Cu at 400 °C [15], and Al6061 sprayed at 200 °C as well as 380 °C [16].

Fig. 7b illustrates the influence of powder strengths, i.e. via as-atomized/ stored or solution heat-treated conditions, on the respective thresholds for reaching the CS bonding regime at the optimized set of parameters (p_{gas} = 3 MPa, T_{gas} = 500 °C) for the given particle sizes (D10 = 13 µm, D50 = 30 µm, and D90 = 52 µm). The comparison of p_{AA} and p_{AS} demonstrates that the powder heat-treatment as applied in the present work, can lead to a significant decrease in critical velocities. The particle impact conditions for the applied particle sizes by higher excess surpassing critical velocities should result in a more pronounced ASI and a higher η [23]. In general, smaller particles, due to their lower inertia, can be accelerated to higher velocities than larger ones. The impact temperatures are determined by heating and cooling during the pass along the nozzle. As sufficiently high temperatures before passing the nozzle throat can be guaranteed for all sizes, the larger particle by their higher thermal momentum and less cooling in the expanding regime, impact at higher temperatures than the smaller ones. However, due to not sufficient heating time to reach the gas temperature by using an injection distance of 35 mm, the larger particles (D90) show rather low impact temperatures. Thus, in the case of p_{AA} with higher v_{crit} the smallest (D10) and the largest (D90) just reach conditions for bonding, while the particles of

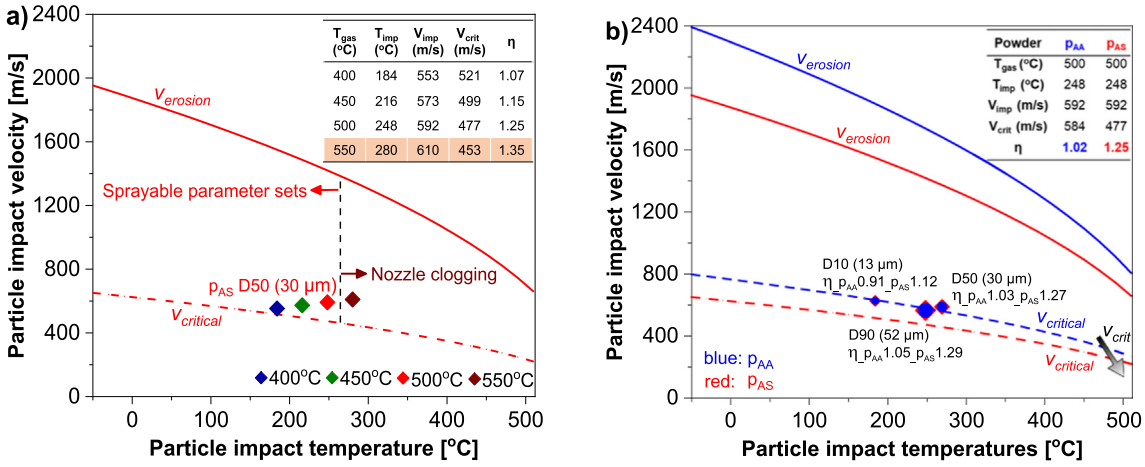

Fig. 7. Particle impact conditions calculated by KSS software for cold spraying; (a) p_{AS} particles (D50 = 30 µm) for cold spraying with N_2 at process parameter sets of p_{gas} = 4 MPa, T_{gas} = 400, 450, 500 and 550 °C. Nozzle clogging occurs at T_{gas} = 550 °C; (b) Particle impact conditions and critical velocities for cold spraying of p_{AA} (blue curves) and p_{AS} (red curves) powders (D10 = 13 µm, D50 = 30 µm, D90 = 52 µm) with N_2 at an optimum parameter set of p_{gas} = 3 MPa, T_{gas} = 500 °C. The inserts in a and b summarize the key data on individual impact conditions.

mean sizes (~D50) meet the right compromise between high velocities and thermal softening to allow for most successful impacts. In contrast, all particles of the soft p_{AS} powder, due to the lower strength, will sufficiently exceed v_{crit} for building up deposits at the spray parameter set with p_{gas} = 3 MPa, T_{gas} = 500 °C, guaranteeing better deposit properties at an η-value of about 1.25. The only disadvantage of the present setup is given by the non-sufficient pre-heating of the largest p_{AS} particles. With rather low impact temperatures, they do not benefit from the decrease of v_{crit} by thermal softening and cannot compensate for their lack of velocity. Thus, the larger p_{AS} particles impact at a slightly lower η-value than the mean-sized ones.

3.3. Deposit microstructures and electrical conductivities

As-solutionized Al6061 powder with homogenized microstructures was used to reveal the influences of the process gas temperatures on the deposit characteristics. The p_{AA} sample deposited under the optimum spray parameter set was included for comparison. Eight spray layers were applied to obtain sufficient deposit thickness for further analyses. The following describes the relationships between the deposit porosity as well as electrical conductivity and individually attained η-parameters.

Fig. 8 correlates deposit porosities and conductivities with the η-parameters attained under different spray conditions. In the case of different p_{AS} deposits, as plotted in Fig. 8a, the porosity is likely to increase and then decrease linearly with increased η-value, which is not in total agreement with related work on the established η-concept [3,18]. At similar deposition efficiencies, the sample processed on basis of the p_{AA} powder shows a lower porosity than the one that had been sprayed with the annealed p_{AS} feedstock, here deposited at T_{gas} of 400 °C. This might be attributed to the peening effects by non-successful particle impacts at lower deposition efficiencies [24]. In addition, it might be noted that for the conditions at low-η regimes (compare 1.07 and 1.02 in Fig. 7), individual impact temperatures for p_{AA} and p_{AS} differ. The particle impact temperature being higher in the case of CS the as stored powder p_{AS}, could indicate that velocity is not always compensating influences of possibly favorable impact temperatures (see Fig. 7a). Further investigations are still required to distinguish the possible effects of the oxide layer, recovery and dynamic recrystallization (DRX), and thermal softening behaviors.

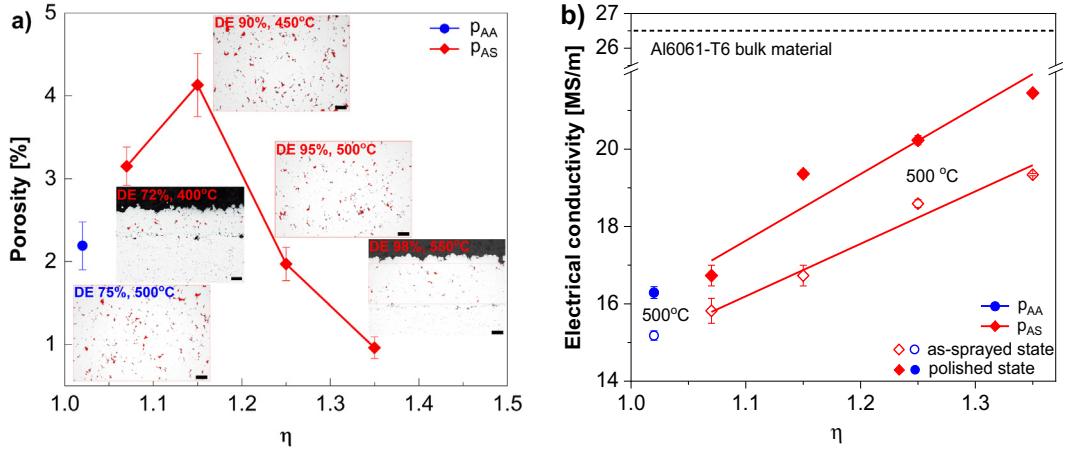

Fig. 8. Al6061 deposit porosities and conductivities for different spray parameter sets and powder states, (a) Correlation between porosities and η-values. The inserts show micrographic images; the scale bar corresponds to 100 µm. In addition, the inserts provide information on spray conditions and obtained deposition efficiencies DE. (b) Correlation between electric conductivities and η-values for as-sprayed and polished surface topographies. Data of an Al6061-T6 plate is included for comparison.

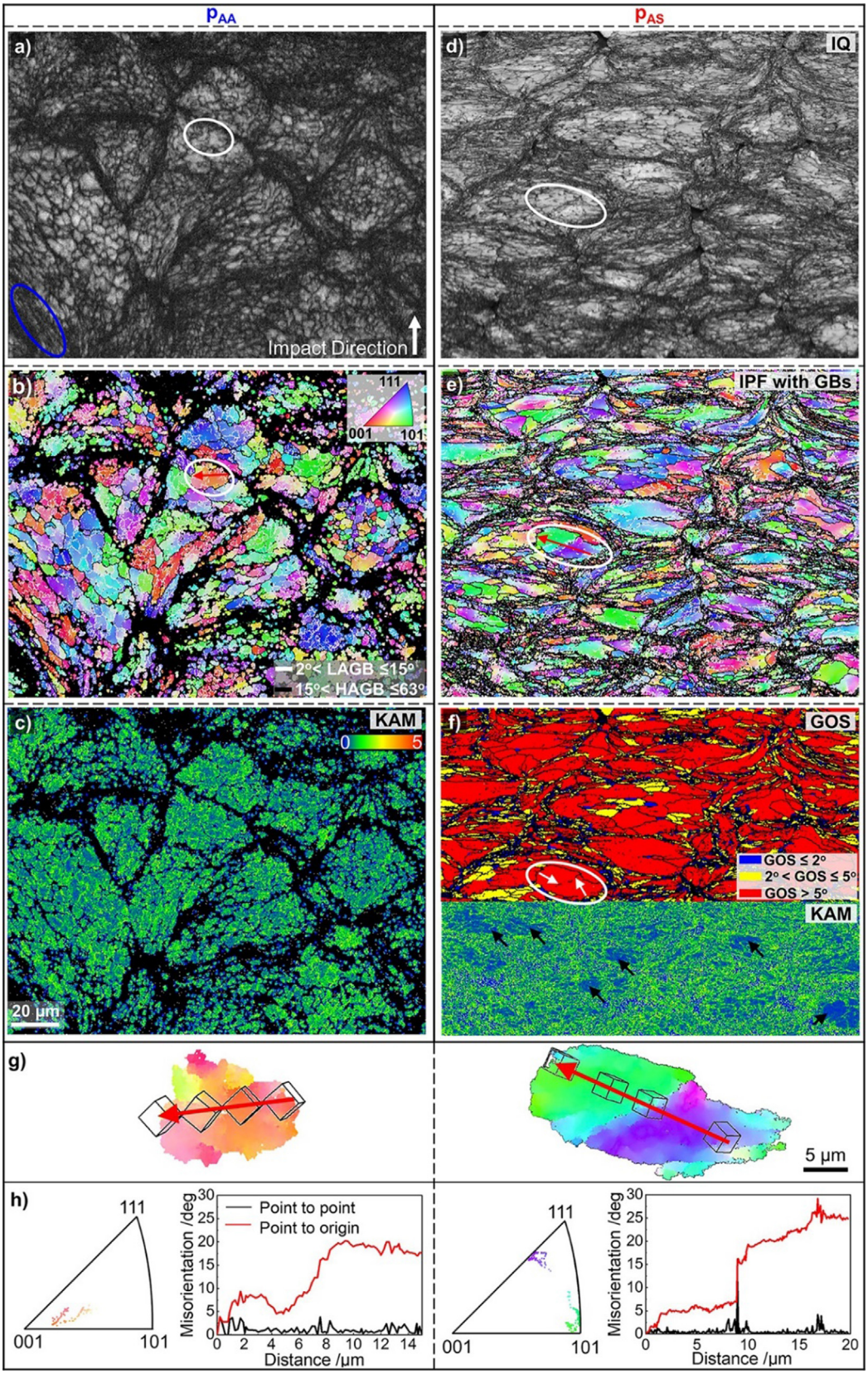

Fig. 9. EBSD analyses of as-fabricated Al6061 deposits by (a-c) p_{AA} powder and (d-f) p_{AS} powder. (a, d) EBSD IQ maps. (b, e) EBSD IPF maps with denoted grain boundaries. (c) EBSD KAM corresponding to Fig. a. (f) EBSD KAM map (below) and GOS map (up) corresponding to Fig. (d). The white circled regions illustrate single deformed grains in (b, e) as highlighted in Fig. g. Fig. h illustrates the misorientation profiles and inverse pole figures in the paths along the red arrowed lines from particle-particle boundaries to center. The red line segment through the single grain from particle-particle interface to center illustrating the angular misalignment roughly perpendicular to impact direction.

Electrical conductivity highly depends on the amount of bonded particle–particle interfaces. Thus, the conductivity was analyzed as an additional measure for the influences of spray conditions and powder states on deposit characteristics. The results given in Fig. 8b are summarized as follows:

i) Electrical conductivity depends on the surface topographies of deposits. Thus, analyses of rough as-sprayed surfaces show slightly lower conductivities than those of the polished ones. The nearly constant difference between as-sprayed and polished surfaces can be attributed to cavities under the sensor and less effective volume of material being subject to induction of eddy currents.

ii) Higher spraying parameter sets, corresponding to higher η, result in higher electrical conductivities of deposits. Nevertheless, the conductivity of the p_{AA} sample sprayed with maximum η at 550 °C reaches only 79% of conductivity observed in the reference Al6061-T6 bulk material (26.5 MS/m). For the rough as-sprayed surface, the electrical conductivities show a similar linear increase over η as those of the polished ones. The electrical conductivity measured on the polished surfaces shows a slightly larger scatter.

iii) Conductivities of softening annealed powder and as atomized/stored hard powder follow the same trend with respect to η. The effect of softening annealing (p_{AS}) against the hard powder (p_{AA}) becomes obvious by comparing the electrical conductivities for both materials processed at T_{gas} = 500 °C. The increase from η = 1.02 by using p_{AA} powder to η = 1.25 for the p_{AS} powder rises the electrical conductivities by about 21%. The comparison between porosities and conductivities demonstrates that low porosities do not necessarily correspond to good coating qualities by high amounts of well-bonded internal interfaces.

To supply more information for the relationship between deposit microstructures and powder conditions, EBSD maps were used to reveal the lattice deformation and distributions of grain sizes and misorientation from particle-particle interface to particle center. Fig. 9 depicts the typical cross-sectional EBSD microstructures of Al6061 deposits by using p_{AA} and p_{AS} as powder feedstock, as fabricated under an optimum spray parameter set (p_{gas} = 3 MPa, T_{gas} = 500 °C).

For both powders, single splats within the deposits can be easily distinguished as shown in the EBSD image quality (IQ) maps (Fig. 9a and 9d). The comparison shows that splats within the p_{AS} deposit are more flattened than those of the p_{AA} one. The lack of indexing resulting in dark contrast at the particle–particle interface is due to the poor Kikuchi pattern quality by severe lattice distortion, as denoted by the blue circle. Locally better pattern quality in the case of the p_{AS} deposit allows detecting refined grains at the internal interfaces and even rare pores at some of the interface triple points.

Fig. 9b and 9e display the orientation distribution maps and illustrate the individual grain sizes and possible distortion within the individual particle splats. The p_{AA} deposit mainly retains the cellular/dendritic networks from the powder atomization with a prevalent fraction (84%) of low-angle grain boundaries (LAGBs). In contrast, the p_{AS} deposit shows a highly deformed microstructure and a significantly lower amount of LAGBs (45%). Moreover, in the case of p_{AS}, the splat interior shows a bimodal grain size distribution with a large population of fine grains at the splat interface that surround areas with coarser grains of the particle interior. Further information on the strain analysis of deposits can be given by the analyses of the kernel average misorientation (KAM), as illustrated in Fig. 9c and 9f. The observations demonstrate that the p_{AS} deposit shows a more uniform plastic deformation and larger areas with low local misorientation (see black arrows in Fig. 9f). The grain orientation spread (GOS) map in Fig. 9f reveals the refined grains in the highly deformed interface areas (highlighted in blue for a GOS of $\leq 2°$). This is attributed to recovery and recrystallization (dynamic/thermal). Due to the high stacking fault energy of Al [25–27], recovery and DRX during CS should be more prominently promoted by the high dislocation densities reached under the low powder strength of p_{AS}. In addition, locally higher temperature by deformation can support following thermal recrystallization and grain growth.

Generally, the orientations of an individual grain should be rather uniform. However, they may vary, particularly, in a deformed regime. To unveil the orientation and deformation-induced lattice rotation in typical examples of single grains of the p_{AA} and the p_{AS} deposits (Fig. 9g), the misorientation angle to the reference point and the orientation gradient along a certain line segment, as well as the transformed inverse pole figures (IPFs), are plotted in Fig. 9h. The lattice rotation along the lines is also illustrated using the orientations of the FCC crystal cubes. The comparison reveals a higher gradient of internal misorientation within the single grain for the p_{AS} deposit than the one for p_{AA}. In addition, the orientation analyses could depict LAGBs inside the p_{AS} grain. As indicated by IPF, the ⟨1 1 1⟩ orientation at the distance of 9 μm from the interface sharply changes to somewhat close to ⟨1 0 1⟩. However, such internal HAGBs are not predominant and only present a small number, as denoted by white arrows in Fig. 9f. More information for the comparison is provided by the orientation changes.

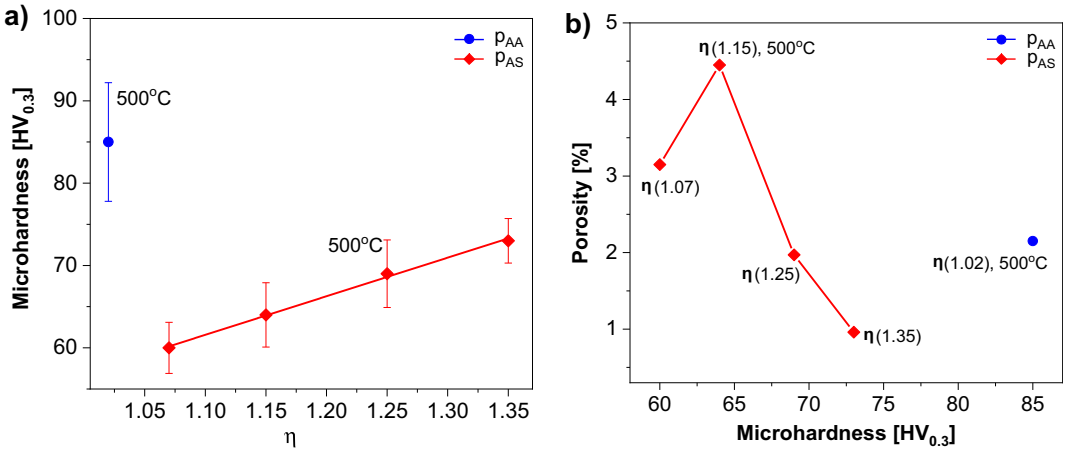

Fig. 10. Influences on deposit hardness: (a) Correlation between microhardness and η-values; (b) Correlation between microhardness and porosity.

They reveal that lattice strain and internal deformation are more prominent for the highlighted p_{AS} grain as common for the overall deposit (compare IPFs in Fig. 9b and 9e) than for p_{AA} deposit.

In summary, the main differences between the p_{AA} and p_{AS} deposits concern splat shape and internal grain deformation, which both can be attributed to the individual mechanical behavior during particle impact. In the following, the associated macroscopic properties will be correlated with detailed microstructural differences.

3.4. Mechanical properties of deposits

3.4.1. Deposit microhardness

This section explores the correlations between calculated quality parameters η and deposit properties, e.g. microhardness and UTS. Fig. 10a shows the obtained microhardness over the different η-values and illustrates that the microhardness of p_{AS} deposits increases with increasing η-value. To a certain extent, this is consistent with the lower porosities reached at higher η-values

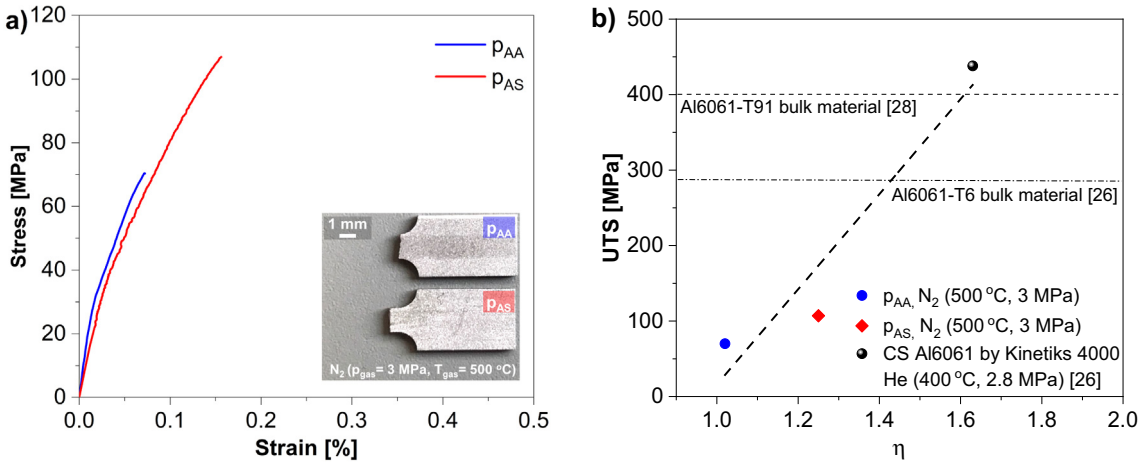

Fig. 11. (a) Stress vs. strain curves obtained by MFT testing. The blue and red curves represent the deposits produced at T_{gas} = 500 °C by spraying p_{AA} and p_{AS} powders, respectively. The insert shows macrographic images of the fractured samples; (b) tensile strength of as-sprayed Al6061 deposits as a function of the η ratio. For comparison, data of the Al6061-T6 [26] and -T91 [28] bulk materials are included in the graph.

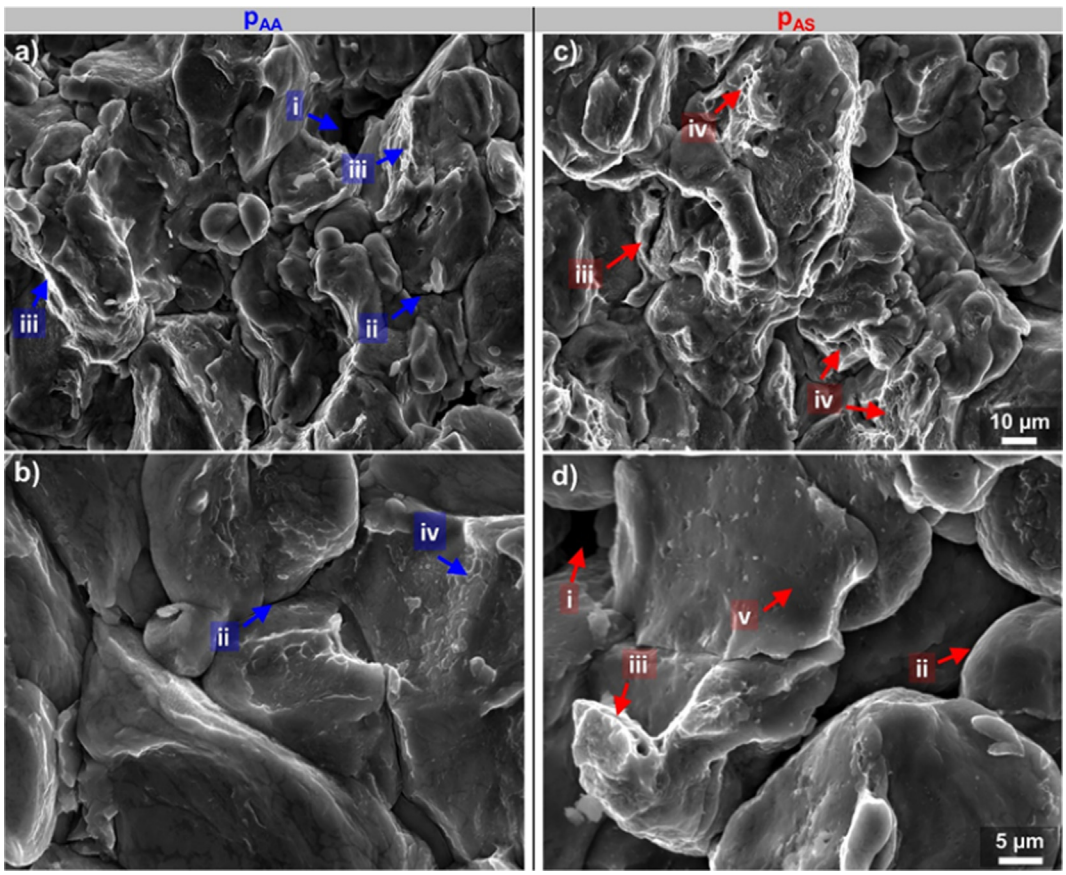

Fig. 12. SEM fractographic images of CS Al6061 deposits of (a-b) p_{AA} and (c-d) p_{AS}. The inserts describe i: porosity, ii: non-bonded interfaces, iii: rupture in well-bonded areas showing low strain, iv: dimples after fracture, and v: splat with high plastic deformation.

(Fig. 10b). In addition, also effects of strain hardening can contribute to higher hardness. In the comparison of the two powders, it becomes obvious that the microhardness of the p_{AA} deposit fabricated at T_{gas} = 500 °C is significantly higher than that of the p_{AS} deposit sprayed under identical conditions. That can be attributed to the higher intrinsic strength of the precipitation-hardened microstructure of the feedstock material p_{AA}.

3.4.2. Deposit strengths and fracture modes

The results on tensile testing are summarized in Fig. 11, which shows typical examples of the stress–strain curves for the p_{AA} and p_{AS} deposits by using the optimized parameter set (T_{gas} = 500 °C). Both samples fail within the elastic regime. However, with 107 MPa the p_{AS} deposit reaches about more 30 % higher strength and elongation at break than the p_{AA} one with 70 MPa. The macroscopic appearance of the fractured samples (see inset in Fig. 11a) gives no evidence for plastic deformation and indicates a rather brittle fracture.

Fig. 11b compares the UTS of the Al6061 deposits from the current work with results reported in the literature. The comparison shows that the UTS roughly follows a linear correlation with η. However, for reaching bulk-like deposit performance, helium as process gas would be needed to establish the required amount of well-bonded interfaces [26]. For the case of CS of Al6061 with helium as process gas, a higher strength in comparison to bulk material under T6 temper conditions is obtained. This can be

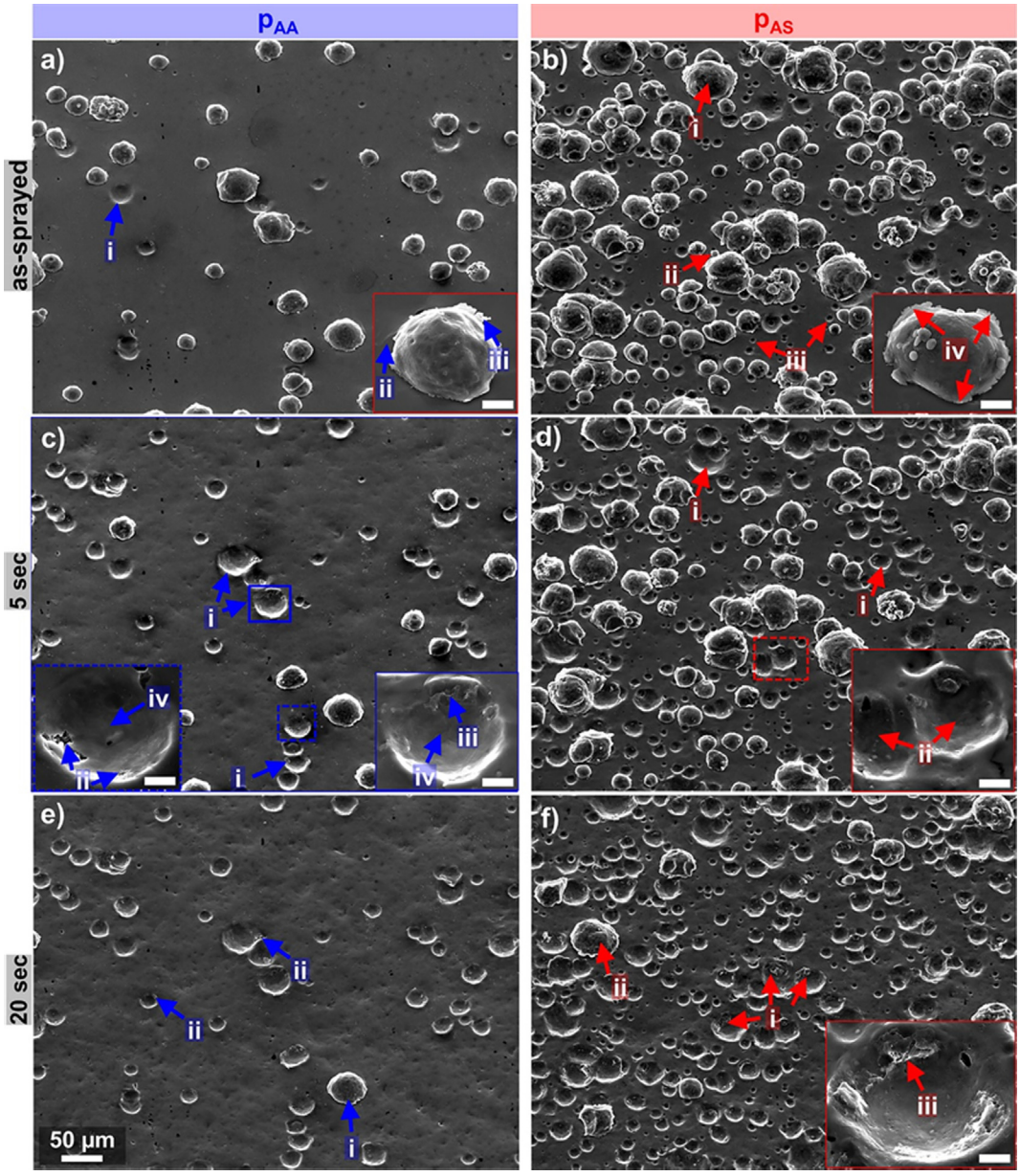

Fig. 13. Surface morphologies (angular views) of wipetest samples sprayed at T_{gas} = 500 °C (left: p_{AA}, right: p_{AS}) on the polished $AlMg_3$ substrates showing the same areas and subsequent particle removal for increasing cavitation exposure times with (a and b): as-sprayed states, and (c and d): 5 sec, and (e and f) 20 sec, respectively. The inserted SEM micrographs in a and b show details of impact morphologies. The inserted SEM micrographs in c, d and f reveal details of the crater after removing originally bonded particles by cavitation. The arrows indicate: (a) i: crater by rebound particle during CS, ii: deformation of the substrate at the periphery of the splat, iii: ASI at the outer rim of particle, (b) i: large splat, ii: small adhering particle, iii: small craters by rebound particle during CS, iv: ASI of particle, (c) i: crater after particle removal by cavitation, ii: rupture side in the crater, iii: particle remnants, iv: centre of crater, (d) i: removed particle holes after cavitation, ii: centre of crater, (e) i: adhering particle after 20 sec cavitation treatment, ii: failure of substrate, (f) i: particle remnants, ii: adhering particle, iii: details with particle remnants. The scale bars in the inserts represent 10 μm.

attributed to the high degree of work hardening, in good agreement with data for T91 temper [28].

Fig. 12 summarizes the fractographic images of Al6061 deposits sprayed at T_{gas} = 500 °C. Fig. 12a-b show the typical fracture surfaces of the p_{AA} deposit and reveals crack branches appearing as traces of porosity (i), non-bonded interfaces (ii), rupture of work-hardened areas (iii), or even dimples after fracture (iv). In contrast, the fracture surfaces of the p_{AS} deposit shown in Fig. 12c, reveal more rupture fracture (iii) and dimples (iv), in good agreement with the higher UTS (Fig. 11a). The higher magnification in Fig. 12d reveals more details of a splat with high plastic deformation (v) and microstructural defects like porosity (i) and non-bonded interfaces (ii) for the p_{AS} deposit.

3.5. Single impact splat adhesion by cavitation-induced erosion

The formation of ASI by high strain-rate deformation between particle and substrate or adhering deposit layers is the necessary pre-requisite for bonding of metallic particles [3]. With increasing particle impact velocity, the range of ASI areas extends from the circumference of the splat towards the centre. For providing information about bonding features, associated with ASI, such as jetting, impact morphologies can supply important information on local particle and substrate deformation as well as on possible failure mechanisms. However, for investigating the extend of ASI, individual particles must be removed.

3.5.1. Cavitation behavior

The splat-to-substrate adhesion strength is one of the key factors affecting the properties of cold sprayed deposits [29]. Single impact adhesion of p_{AA} and p_{AS} particles was analyzed by particle detachment under cavitation testing and respective statistical data evaluation. The surface morphologies of the as-sprayed state and after 5 and 20 sec of cavitation treatment are shown in Fig. 13. The quantitative data, e.g., the size distributions of adhering particles and craters in the as-sprayed state and the amount of adhering particles after 5, 10 and 20 sec of cavitation treatment, are summarized in Fig. 14 and Fig. 15, respectively.

Fig. 13a-b show the surface and impact morphologies of as-atomized and as-solutionized powders, respectively, as obtained by CS under p_{gas} = 3 MPa and T_{gas} = 500 °C on polished $AlMg_3$ substrates. The results from statistical analyses of impact morphologies in the as-sprayed state are summarized in Fig. 14. This comparison shows the size distributions of powders, splats and craters left after the impact of p_{AA} and p_{AS} powders. For both, the dimensions of craters and splats appear smaller than the mean diameter of the original powder material (black curve). In the case of p_{AA}, a narrow splat size distribution (solid blue curve) and a large crater size distribution (dashed blue curve) are observed (see arrow i in Fig. 13a). In comparison to that, the deposition of p_{AS} results in a slightly broader splat size distribution (compare also arrows of i and ii in Fig. 13b) and smaller crater sizes (see arrow iii in Fig. 13b).

When observing the single impact morphologies at higher magnification, the substrate deformation is visible for the p_{AA} impacts (see arrow ii in the inset of Fig. 13a). ASI is indicated by 'iii' in Fig. 13a and 'iv' in Fig. 13b. The extend of ASI seems to be higher for the p_{AS} impacts than for p_{AA}. In the as-sprayed state, only a few empty craters are left on the substrate surface by non-successful impacts. For the same areas, subsequent particle removal can be followed for increasing cavitation exposure times. However, with increasing cavitation time, most of the originally adhering particles are removed. The particle removal appears to be more prominent for p_{AA} single impacts. For example, after 5 sec of cavitation testing, as shown in Fig. 15, the wipetest samples underlie a particle loss of about 65% for the p_{AA} powder, which is higher than the 59 % loss of the p_{AS} specimen. For the failure topography of the p_{AA} wipetest sample after 5 sec (Fig. 13c), holes by already removed particle under cavitation (arrow i), localized fracture in the holes (arrow ii), particle remnants (arrow iii) and most prominently clean crater areas (arrow iv) are observed, while no clear failure in the caters for p_{AS} sample (Fig. 13d). After an increase of cavitation time to 10 sec (Fig. 15), the respective amount of particle loss is about 85% and 80% for the two wipetest samples of p_{AA} and p_{AS}, respectively. Comparing the details of fracture sites after particle removal of 20 sec, the p_{AS} powder more prominently leaves particle remnants in the empty craters (see arrows i, iii in Fig. 13f). In contrast, the bonded p_{AS} particles are more prominently detached by failure on substrate sites (see arrows ii in Fig. 13e). In summary, the comparison of the cavitation behavior between the two wipetest samples, the one sprayed by p_{AS} by ensuring higher η results in slightly better adhesion of single particles, as quantitatively analyzed by the cumulative loss of splats during cavitation testing (Fig. 15).

3.5.2. Detached particles

Collected particles after removal by cavitation testing can provide valuable information on possible failure modes at the interface. Fig. 16 shows typical examples for the p_{AA} and p_{AS} splats.

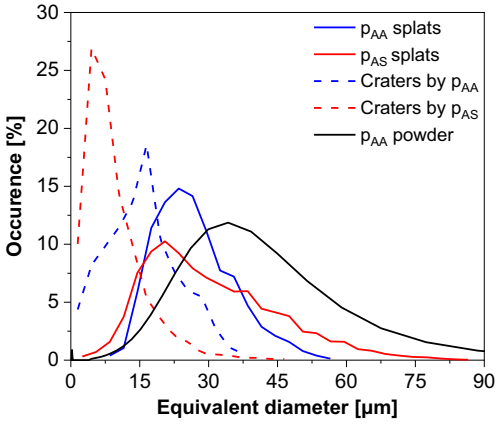

Fig. 14. Statistical analyses of impact morphologies: size distributions of adhering splats and craters according to the quantitative analysis on the angular view of the wipetest samples in the as-sprayed state at T_{gas} = 500 °C, p_{gas} = 3 MPa. The colored solid and dashed lines represent the splat and crater, respectively.

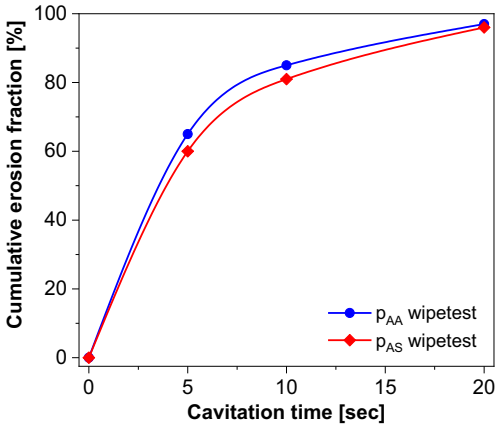

Fig. 15. Cumulative erosion fraction of the adhering particles as a function of cavitation time for wipetest samples sprayed with p_{AA} (blue) and p_{AS} (red) powders at T_{gas} = 500 °C, p_{gas} = 3 MPa.

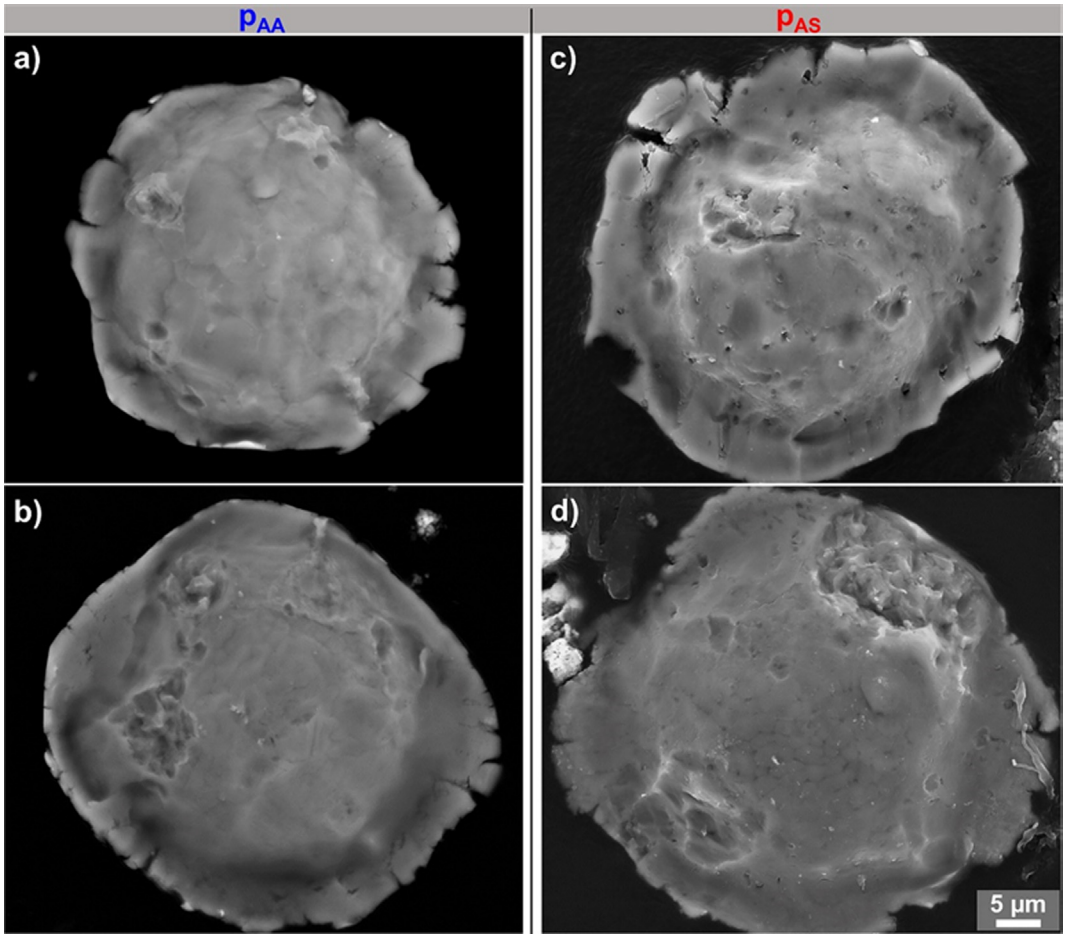

Fig. 16. SEM micrographs of the detached particles: (a-b) p_{AA} and (c-d) p_{AS}, as obtained by cavitation testing on wipetest samples (corresponding to Fig. 13).

All of them show jetting at the periphery of the splats and clean surfaces and no traces of severe interface deformation at the centre of the contact zone to the substrate. By the lower particle strength, jet formation appears more pronounced for p_{AS} splats.

According to these examples, the interfaces of p_{AS} more prominently fail at the substrate, whereas the p_{AA} splats show more failure within the particle interior next to the bonded interfaces. This can be attributed to differences in individual powder strengths at impact temperature and substrate strengths under the applied work hardening.

4. Discussion

4.1. Effects of annealing on powder microstructures and properties

Analyses on powder morphologies and sizes showed that the general appearance of the Al6061 powder is retained after the heat-treatment. Only a minor increase in oxygen content could be obtained. Stable oxide layers on Al-alloy powders could have different consequences on powder modification by annealing and cold spraying. On the one hand, for powder annealing, the oxide layers are beneficial for avoiding sintering [9]. On the other hand, such oxide layers could hinder the mechanisms for CS deposition, as demonstrated by various investigations [19–21,30]. A possibly higher oxygen content of the feedstock powder results in an increased v_{crit} and thus reduces deposition efficiency and amounts of bonded particle interfaces. According to literature, the natural oxygen content of gas-atomized Al powders typically ranges from 0.074 to 0.15 wt% [9,31]. Thus, the measured oxygen contents for the p_{AA} and p_{AS} powders are still comparable to the reported data, confirming the good conditions for powder storage and powder solutionizing.

The observed non-equilibrium microstructure with continuous networks of secondary-phases is typical for supersaturated Al alloys exposed to rapid undercooling rates of up to 10^5 K/s in powder atomization [9]. Similar microstructural features for gas-atomized Al alloy powders have also been reported in the literature [13,15,16,17]. A detailed example is given by Bedard et al. [16]. The authors could distinguish two different secondary phases segregating at cell boundaries by STEM-EDXS analysis, one consisting of Mg_2Si, and the other one as Fe-rich phase alloyed with Si and low Al content. In agreement with that, Tsaknopoulos et al. [17] showed that precipitate distributions at interdendritic boundaries in as-atomized Al6061 powder consist of β-Mg_2Si phases within a Fe-rich phase surrounding. Boundaries between cell colonies with identical orientation correspond to the grain boundaries [13,16], which was also demonstrated by the EBSD data in Fig. 9b.

Sabard et al. [11,13] reported a decrease in powder hardness after solution heat-treatment. This shows that homogeneously distributed fine precipitates in the as stored samples act as sufficient dislocation barriers to cause higher strengths. Elevated temperatures reaching the solution range of the Al α-phase allow for the dissolution of precipitates into the host matrix. Therefore, the strength of as stored powder (here p_{AA}) can be expected to be decreased by homogenization. In contrast to the pronounced partitioning and secondary phases being presented at interdendritic/-cellular boundaries in the p_{AA} powder, such features get less

prominent after the heat-treatment, as observed in the p_{AS} powder. The dissolution of partitioned areas not being complete can be probably related to either short annealing times or the occurrence of rather stable phases at these boundaries, in accordance with the results reported in the literature [13–15,17]. Detailed analyses of changes in composition and phase evolution surrounding the sub-grain boundaries in Al6061 powder after solution treatment were investigated by Tsaknopoulos et al. [17], indicating a decreasing content of Mg_2Si from 1.62% to 0.81% and increasing Fe-rich phase content from 3.42% to 4.4%, respectively. As revealed by Bedard et al. [16], the majority of solute atoms, such as Mg and Si, were dissolved into Al matrix, while Fe-rich phase becomes more prominent, associated with coarsening and spheroidization. The growth of Fe-rich phase is similarly observed for p_{AS} powder in Fig. 4c-d.

The particle compression test is a reliable tool to determine powder strengths and to allow for more accurate descriptions of critical conditions for successful deposition in cold spraying. As compared to other techniques as the compression testing of micro-pillar (with a diameter of 5 μm) [7,16], the global deformation of whole particles is less influenced by local microstructures, grain boundary distributions, or local anisotropies [8]. A lower YS/UTS ratio means that the p_{AS} condition allows for more strain hardening during plastic deformation before failure. In addition, the results on powder morphologies after compression indicate some anisotropy. Such would be expected for rather large, nearly single crystalline particles by mainly activating dislocations on slip systems with the highest Schmid-factor. In accordance, Sousa et al. [32] reported significant differences in the particle hardness of as-atomized Al6061 powder as a function of grain orientation.

4.2. Strategies to optimize CS for Al 6061-deposits

Ideally, cold sprayed deposits could reach properties similar to those of respective bulk materials [2,3]. However, in the case of Al6061, attainable deposit properties are impeded by rather high material strength and practical restrictions to access needed processing parameter regimes.

According to literature data for CS of Al6061 deposits by using N_2 as process gas, a high porosity usually occurs due to insufficient particle plastic deformation [15,33,34]. For example, Aldwell et al. [34] reported a high porosity of Al6061 deposit produced by N_2 (T_{gas} = 400 °C, p_{gas} = 2 MPa) of about 8%. By cold spraying with N_2 as process gas, high process temperatures are needed for providing sufficiently fast gas and thus particle velocities, as well as particle preheating to enhance deformation by thermal softening [33]. However, a higher gas temperature of T_{gas} = 550 °C already leads to nozzle clogging. Impact conditions with similarly high η-value ≥ 1.35 can be obtained by using helium as process gas, as given in Table 3.

By higher velocities of gas and thus particle velocities, the use of He allows operating at much lower gas temperatures (T_{gas} = 55 °C), and avoids problems with nozzle clogging. Despite the high costs of He, this route is followed by many investigations [10,11,13,14,16,25,26]. In contrast, softening annealing of the as-atomized powder before CS represents an alternative approach to reach high η-values just by the reduced critical velocities for bonding, as indicated in Fig. 7b, to ensure economic deposit build-up. In the present work, optimized η-values within the attainable parameter regime by using softened powder p_{AS} can reduce porosities to less than 1 ~ 2%.

Table 3
Particle impact conditions for CS of p_{AS} with helium at the lower process parameter sets of p_{gas} = 1.5 MPa, T_{gas} = 155 °C, showing the same η (1.35) as for CS with N_2 at a process parameter set of p_{gas} = 3 MPa, T_{gas} = 550 °C (refer to Fig. 6a), that causes nozzle clogging.

T_{imp} (°C)	v_{imp} (m/s)	v_{crit} (m/s)	η
−41	881	651	1.35

4.3. Influences of annealing on the window for particle deposition

The amount of particles that within a given sizes distribution adhere to the substrate or the already deposited spray layer in CS is determined by the individual excess over η of 1. At given parameter sets, the attainable impact velocities, as well as the critical velocities, depend on the particle sizes. As an example, for a selected process condition (N_2, p_{gas} = 3 MPa, T_{gas} = 500 °C), η is here given as a function of particle size, as shown in Fig. 17. With increasing particle size, η increases first and then turns to decrease. When spraying p_{AA} powder, the particle size range for effective deposition is rather narrow, as denoted by the solid blue line. In the case of the higher critical velocities of the harder p_{AA} powder, the impact velocities of smaller size particles do not exceed the critical velocities for bonding shown as indicated by the solid green line. In contrast, by the lower critical velocity of the softening annealed p_{AS} powder, all sizes of the given batch should exceed needed conditions for bonding, as revealed by the solid red line. This also can be proved by the single-particle impacts, as shown in Fig. 13a-b and 14. This approach thus explains that significantly higher deposition efficiencies can be obtained by using softening annealed powder instead of room temperatures aged ones.

4.4. Effects on deposit microstructures and properties

For the lower η-values (<1.1), deposit porosities do not follow the same tendency as seen for higher η-values (Fig. 8b). In contrast, the electrical conductivity increases linearly with η (Fig. 8b). This discrepancy can be explained by densification of deposits at a lower DE (72% and 75%) under peeing effects by rebounded big particles [24]. Such is evidenced by the larger crater size and the smaller splat size in Fig. 14. Obtaining smaller conductivities at low porosities can be attributed to pores that by non-successful impacts get compressed to micro-cracks. This fact is supported by smaller amounts of dimple-sites on the fracture surface (Fig. 12) and smaller ASI areas on the removed splats (Fig. 16) for using the p_{AA} powder. The well-bonded interfaces of the soft

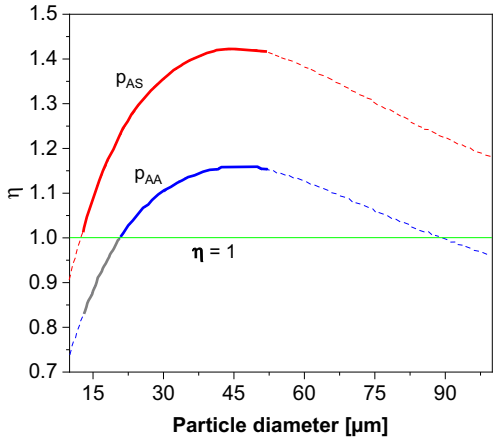

Fig. 17. η (considering the particle strength) as a function of the particle diameter over Al6061 particle sizes during CS under optimum parameter sets of T_{gas} = 500 °C and p_{gas} = 3 MPa. The calculations assumed a powder injection distance of −35 mm upstream of the nozzle throat. Blue and red curves represent p_{AA} and p_{AS}, respectively. The powder size distribution (13–52 μm) used in this work is marked in the graph by solid lines.

p_{AS} particles are attributed to a higher amount of ASI by thermal softening as obtained at the lower critical velocity (477 m/s, Fig. 7b) during CS. The thermomechanical history then determines the recovery and dynamic + possibly thermal recrystallization behavior as shown by EBSD results. Respectively more dimple patterns are observed in the fractured surface (Fig. 12c), confirming further ductile behavior, which is in good agreement with refined grains at particle–particle interfaces in Fig. 9f. However, it should be also pointed out that a possible lack of well-bonded areas can be caused to the possible presence of oxide films. Such should apply to p_{AA} by storage and be enhanced for p_{AS} powder by later heat-treatment.

Although p_{AS} shows a more uniform microstructure, the details of strengthening mechanisms in CS of annealed powder remain complicated [26]. On one hand, the higher strain-rate deformation associated with higher η-value leads to higher dislocation densities during CS, as confirmed by the higher splat flattening with more internal grain misorientation (Fig. 9e and 9 g). Due to a high level of solute atoms dissolved into the Al matrix in p_{AS} powder, a certain quantity of nanoscale phases might precipitate, thus by strengthening increasing local nano- or microhardness. On the other hand, the increased spraying parameters also result in local hardness decreases due to thermal softening by recovery and recrystallization. Also, by short-time storage occurring precipitates in p_{AS} powder can still offer a strengthening effect. In addition, possible oxide films impede particle deformation and possible jetting [34]. Thus, apart from hardening by natural aging, also storage conditions play a significant role in attainable deposit performance and explain the UTS for the produced deposit by p_{AS} showing a lower UTS than expected.

For testing conditions under compression, the microhardness can be used as a global measure for yield strength and work hardening by cold working [34], indicating a higher strength of the p_{AA} deposit (85 $HV_{0.3}$) than for the p_{AS} sample (69 $HV_{0.3}$). However, under tension, the situation is different. Here, the strength of deposits is generally restricted by the amounts and sizes of internal defects, like porosity, oxides and non-bonded interfaces [4]. In the present case, the real ratio of the well-bonded interfaces to the overall interface areas in p_{AS} deposit can be estimated to be higher than that of the p_{AA} deposit, which correlates well with higher electrical conductivities, see Fig. 8b. Therefore, the real η determined by powder strength could provide a more reliable property prediction; a higher η-value leads to more bonded interfaces and thus better deposit quality.

5. Summary and conclusions

A route of powder-process-performance integrated cold spraying of Al6061 is described for enhancing deposit performance. The present work presents influences of solution heat-treatment on the microstructures and key properties of as-atomized particles and their effects onto needed process parameters sets for reaching sufficiently high excess above critical velocities. Attained consequences by using as-atomized and as-solutionized powders as feedstock for CS are described by differences in microstructures and properties of Al6061 deposits, as well as by cavitation behaviors of single-particle impacts. By the lower particle strength and thus lower critical velocities, annealed powders result in higher deposition efficiencies and better deposit properties. The following main conclusions can be drawn:

(a) For CS of Al6061 deposits produced with N_2 as process gas, powder solution heat-treatment can effectively tune the needed properties of particles by decreasing the particle strength.

(b) For correlating the deposit characteristics with the quality parameter η, comparisons within the different deposits by softening annealed powder reveal that the highest η-value ensures the lowest porosities and the highest electric conductivity as well as higher strength.

(c) The comparative analyses on deposits and single particles impacts between as-atomized and softening annealed powders indicate that the easier high strain-rate deformation of the softening annealed particles allows for increased formation of well-bonded areas of ASI and thus better bonding at particle interfaces and in consequence deposit properties.

In summary, the present work allows to derive general knowledge on powder heat-treatment for enlarging sprayability ranges in CS and for defining requirements for CS process parameter sets to adjust needed deposit properties. Thus, the comparison of the behavior of different powder conditions in CS could be interpreted as the primary step to tune these thermally softened materials for possible industrial applications.

Declaration of Competing Interest

The authors declare that they have no known competing financial interests or personal relationships that could have appeared to influence the work reported in this paper.

Acknowledgments

C.J. HUANG acknowledges the financial support of the Alexander von Humboldt Foundation. The authors also acknowledge T. Breckwoldt, M. Kollmeier, M. Schulze and C. Schulze in HSU for support in sample preparation and microstructural analyses.

Appendix A. Supplementary material

Supplementary data to this article can be found online at https://doi.org/10.1016/j.matdes.2022.110494.

References

[1] W. Li, K. Yang, S. Yin, X. Yang, Y. Xu, R. Lupoi, Solid-state additive manufacturing and repairing by cold spraying: A review, J Mater. Sci. Tech. 34 (3) (2018) 440–457.
[2] T. Schmidt, H. Assadi, F. Gärtner, H. Richter, T. Stoltenhoff, H. Kreye, T. Klassen, From particle acceleration to impact and bonding in cold spraying, J. Therm. Spray Tech. 18 (2009) 794–808.
[3] H. Assadi, H. Kreye, F. Gärtner, T. Klassen, Cold spraying - A materials perspective, Acta Mater. 116 (2016) 382–407.
[4] C.J. Huang, M. Arseenko, L. Zhao, Y.C. Xie, A. Elsenberg, W.Y. Li, F. Gärtner, A. Simar, T. Klassen, Property prediction and crack growth behavior in cold sprayed Cu deposits, Mater. Des. 206 (2021) 109826.
[5] C.J. Huang, X.C. Yan, C.Y. Chen, Y.C. Xie, M. Liu, M. Kuang, H.L. Liao, Additive manufacturing hybrid Ni/Ti-6Al-4V structural component via selective laser melting and cold spraying, Vacuum 151 (2018) 275–282.
[6] H. Assadi, I. Irkhin, H. Gutzmann, F. Gärtner, M. Schulze, M.V. Vidaller, T. Klassen, Determination of plastic constitutive properties of microparticles through single particle compression, Adv. Powder. Tech. 26 (2015) 1544–1554.
[7] T.J. Flanagan, B.A. Bedard, A.M. Dongare, H.D. Brody, A. Nardi, V.K. Champagne, M. Aindow, S.-W. Lee, Mechanical properties of supersonic-impacted Al6061 powder particles, Scripta Mater. 171 (2019) 52–56.
[8] H. Assadi, F. Gärtner, Particle compression test: A key step towards tailoring of feedstock powder for cold spraying, Coatings. 20 (2020) 458.
[9] A. Ünal, Production of rapidly solidified aluminium alloy powders by gas atomisation and their applications, Powder Metal. 33 (1) (1990) 53–64.
[10] M.R. Rokni, A.T. Nardi, V.K. Champagne, S.R. Nutt, Effects of preprocessing on multi-direction properties of aluminum alloy cold-spray deposits, J. Therm. Spray Tech. 27 (5) (2018) 818–826.
[11] A. Sabard, H.L. de Villiers Lovelock, T. Hussain, Microstructural evolution in solution heat treatment of gas-atomized Al alloy (7075) powder for cold spray, J. Therm. Spray Tech. 27 (1-2) (2018) 145–158.
[12] A. Sabard, P. McNutt, H. Begg, T. Hussain, Cold spray deposition of solution heat treated, artificially aged and naturally aged Al 7075 powder, Surf. Coat. Tech. 385 (2020) 125367.

[13] A. Sabard, T. Hussain, Inter-particle bonding in cold spray deposition of a gas-atomised and a solution heat-treated Al 6061 powder, J. Mater. Sci. 54 (2019) 12061–12078.
[14] W.A. Story, L.N. Brewer, Heat treatment of gas-atomized powders for cold spray deposition, Metal. Mater. Trans. A 49 (2018) 446–449.
[15] T. Liu, W.A. Story, L.N. Brewer, Effect of heat treatment on the Al-Cu feedstock powders for cold spray deposition, Metal. Mater. Trans. A. 50 (7) (2019) 3373–3387.
[16] B.A. Bedard, T.J. Flanagan, A.T. Ernst, A. Nardi, A.M. Dongare, H.D. Brody, V.K. Champagne, S.-W. Lee, M. Aindow, Microstructure and micromechanical response in gas-atomized Al 6061 alloy powder and cold-sprayed splats, J. Therm. Spray Tech. 27 (8) (2018) 1563–1578.
[17] K. Tsaknopoulos, C. Walde, V. Champagne, D. Cote, Gas-atomized Al 6061 powder: phase identification and evolution during thermal treatment, JOM. 71 (2019) 435–443.
[18] H. Assadi, T. Schmidt, H. Richter, J.-O. Kliemann, K. Binder, F. Gärtner, T. Klassen, H. Kreye, On parameter selection in cold spraying, J. Therm. Spray Tech. 20 (6) (2011) 1161–1176.
[19] M.V. Vidaller, A. List, F. Gaertner, T. Klassen, S. Dosta, J.M. Guilemany, Single impact bonding of cold sprayed Ti-6Al-4V powders on different substrates, J. Therm. Spray Tech. 24 (4) (2015) 644–658.
[20] M. Razavipour, S. Rahmati, A. Zuniga, D. Criado, B. Jodoin, Bonding Mechanisms in cold spray: Influence of surface oxidation during powder storage, J. Therm. Spray Tech. 30 (2021) 304–323.
[21] M. Yu, W. Li, X. Guo, H. Liao, Impacting behavior of large oxidized copper particles in cold spraying, J. Therm. Spray Tech. 22 (2-3) (2013) 433–440.
[22] Heat Treating of Aluminum Alloys, ASM Handbook, Volume 4: Heat Treating, editor by G.E. Totten, ASM International, 2016, 841-879.
[23] T. Schmidt, F. Gärtner, H. Assadi, H. Kreye, Development of a generalized parameter window for cold spray deposition, Acta Mater. 54 (3) (2006) 729–742.
[24] N.S. Fan, J. Cizek, C.J. Huang, X.L. Xie, Z. Chlup, R. Jenkins, R. Lupoi, S. Yin, A new strategy for strengthening additively manufactured cold spray deposits through in-process densification, Addi. Manuf. 36 (2020) 101626.
[25] M.R. Rokni, C.A. Widener, V.R. Champagne, M.R. Rokni, C.A. Widener, V.R. Champagne, Microstructural evolution of 6061 aluminum gas-atomized powder and high-pressure cold-sprayed deposition, J. Therm. Spray Tech. 23 (2014) 514–524.
[26] M.R. Rokni, C.A. Widener, O.C. Ozdemir, G.A. Crawford, Microstructure and mechanical properties of cold sprayed 6061 Al in as-sprayed and heat treated condition, Surf. Coat. Tech. 309 (2017) 641–650.
[27] C. Borchers, F. Gärtner, T. Stoltenhoff, H. Kreye, Microstructural bonding features of cold sprayed face centered cubic metals, J. Appl. Phys. 96 (8) (2004) 4288–4292.
[28] http://www.matweb.com/index.aspx.
[29] Y. Ichikawa, R. Tokoro, M. Tanno, K. Ogawa, Elucidation of cold-spray deposition mechanism by auger electron spectroscopic evaluation of bonding interface oxide film, Acta Mater. 164 (2019) 39–49.
[30] W.Y. Li, H. Liao, C.J. Li, H.S. Bang, C. Coddet, Numerical simulation of deformation behavior of Al particles impacting on Al substrate and effect of surface oxide films on interfacial bonding in cold spraying, Appl. Surf. Sci. 253 (11) (2007) 5084–5091.
[31] S. Özbilen, A. Ünal, T. Sheppard, Influence of atomizing gases on the oxide-film morphology and thickness of aluminum powders, Oxid. Met. 53 (2000) 1–23.
[32] B.C. Sousa, C.E. Walde, V.K.C. Jr, D.L. Cote, Initial observation of grain orientation dependent nanoindentation hardness of Al 6061 gas-atomized powder, Int. J. Metal. Met. Phys. 5 (2020) 050.
[33] Y.K. Wei, X.T. Luo, X. Chu, G.S. Huang, C.J. Li, Solid-state additive manufacturing high performance aluminum alloy 6061 enabled by an in-situ micro-forging assisted cold spray, Mater. Sci. Eng. A. 776 (2020) 139024.
[34] B. Aldwell, E. Kelly, R. Wall, A. Amaldi, G.E. O'Donnell, R. Lupoi, Machinability of Al 6061 deposited with cold spray additive manufacturing, J. Therm. Spray. Tech. 26 (7) (2017) 1573–1584.